Soil Dynamics and Earthquake Engineering 47 (2013) 62–82

Contents lists available at SciVerse ScienceDirect

Soil Dynamics and Earthquake Engineering

journal homepage: www.elsevier.com/locate/soildyn

Site characterization using full waveform inversion

L.F. Kallivokas [a,b,*], A. Fathi [a], S. Kucukcoban [d], K.H. Stokoe II [a], J. Bielak [c], O. Ghattas [b]

[a] Department of Civil, Architectural and Environmental Engineering, The University of Texas at Austin, Austin, TX 78712, USA
[b] The Institute for Computational Engineering and Sciences, The University of Texas at Austin, Austin, TX 78712, USA
[c] Department of Civil and Environmental Engineering, Carnegie Mellon University, Pittsburgh, PA 15213, USA
[d] Stress Engineering Services Inc., 13610 Westland East Blvd., Houston, TX 77041, USA

ARTICLE INFO

Article history:
Received 5 June 2012
Accepted 20 December 2012
Available online 4 February 2013

ABSTRACT

We discuss recent progress in the full-waveform-based imaging of probed soils, with geotechnical site characterization applications in mind. The primary goal is the reconstruction of the material profile of near-surface, arbitrarily heterogeneous formations, in terms of the formation's spatially distributed elastic properties, using elastic waves as the probing agent.

We describe first the formulation and numerical resolution of the underlying time-dependent inverse medium problem; we report briefly on numerical experiments using synthetic data and artificial target soil profiles. These demonstrate robust reconstruction. We then report extensively on the details of a field experiment, whose records we subsequently used to drive the inversion algorithms in order to characterize the site where the field experiment took place. Lastly, we compare the inverted site profile with profiles obtained using the Spectral-Analysis-of-Surface-Waves (SASW) method, in an attempt to compare our methodology against a widely used concurrent inversion approach. We also compare the inverted profile at select locations with the results of independently performed CPT tests.

Overall, whether exercised by synthetic or by physical data, the full waveform inversion method we discuss herein appears quite promising for the robust subsurface imaging of near-surface deposits in support of geotechnical site characterization investigations.

1. Introduction

Geotechnical site characterization refers to our ability to image the properties of the soil within the near-surface deposits, ideally in a non-invasive manner. Imaging the soil shares common elements with imaging in other disciplines, most notably medical imaging, albeit without the benefit that a tightly controlled medical setting affords to imaging. The problem belongs to the broader class of inverse medium problems: waves, whether of acoustic, electromagnetic, or elastic nature, are used to interrogate a medium, and the medium's response to the probing is subsequently used to image the spatial distribution of properties (densities or moduli). Mathematically, algorithmically, and computationally, inverse medium problems are fairly challenging, especially when no *a priori* constraining assumption is made on the spatial distribution of the medium's properties. The challenges are further compounded when the underlying physical problem is time-dependent, as is in the site characterization case.

Because of the inherent complexity of the inversion problem, most of the methods developed to date rely on simplifying assumptions that aim at rendering a solution to the problem more tractable. Most commonly, these simplifications limit the properties' spatial variability: horizontal layering assumptions pervade most site characterization approaches, including the celebrated Spectral-Analysis-of-Surface-Waves (SASW) [19], or its close relative, the Multichannel-Analysis-of-Surface-Waves (MASW) [14]. However, continued advances in both algorithms and computer architectures have allowed the gradual removal of the limitations of existing methodologies.

In this paper, we discuss recent advances in site characterization, based on a full waveform inversion methodology. The seeding concepts of full waveform inversion are not new: the goal is to reconstruct the material profile of a probed soil domain using the *complete* waveforms of its response to interrogating waves (elastic waves). Convergence to the reconstructed property profile is then accomplished by enforcing the minimization of a misfit between observed records of the soil's response and computed records based on trial guesses of the medium's properties. Full waveform inversion methods are the purview of geophysical exploration, where they are still under continuing

* Corresponding author at: Department of Civil, Architectural and Environmental Engineering, The University of Texas at Austin, Austin, TX 78712, USA.
E-mail addresses: loukas@mail.utexas.edu (L.F. Kallivokas), arash.fathi@utexas.edu (A. Fathi), sezgin.kucukcoban@stress.com (S. Kucukcoban), k.stokoe@mail.utexas.edu (K.H. Stokoe II), jbielak@andrew.cmu.edu (J. Bielak), omar@ices.utexas.edu (O. Ghattas).

0267-7261/$ - see front matter © 2013 Elsevier Ltd. All rights reserved.
http://dx.doi.org/10.1016/j.soildyn.2012.12.012

development: a robust methodology, especially for the time-dependent elastic case remains, by and large, elusive. In this vein, the methodology we report here in the context of geotechnical site characterization seems quite promising. Using a full waveform inversion method for site characterization entails additional difficulties, not usually encountered in geophysical exploration, due to the need to limit the extent of the probed domain. To be able to tackle all the difficulties of inverting for the near-surface deposits, we integrate recent advances in several areas; specifically, we use (a) a new forward wave simulation method for domains terminated by perfectly-matched-layers (PMLs), which is suitable for dealing with the limited extent of sites particular to geotechnical investigations [9]; (b) a partial-differential-equation-constrained optimization approach for tackling the inverse medium problem endowed with specialized convergence accelerators [7]; (c) regularization schemes to address solution multiplicity inherent in the inverse problem [4]; (d) a *discretize-then-optimize* implementation scheme to assist the gradient-based optimizer to arrive at the target profile [2,15]; and (e) continuation schemes that improve algorithmic convergence [7,11].

Fragments of the methodology have already been reported elsewhere. Our primary focus here is on the field experiments and on the inversion results that were based on the field data. Nonetheless, we discuss, albeit briefly, all necessary ingredients for inversion. The methodology we present is fairly general: here, we discuss it only in the context of two-dimensional inverse problems. Three-dimensional extensions will be reported in the future.

The remainder of this paper is organized as follows: first, we discuss mathematical and numerical aspects of the underlying inverse medium problem. We report numerical results using synthetic data, which serve to provide early justification for the methodology. Next, we discuss details of the design of a field experiment aimed at collecting physical data in a manner suitable for exercising the methodology. We then report on the field experiment, and the resulting site characterization using real data and the full waveform approach. We compare the rendered site profile against profiles obtained using the SASW, and report on localized CPT tests that reinforce the validity of the profile. Lastly, we conclude with summary remarks.

2. Problem definition

To fix ideas, we refer to the depiction of the driving application shown in Fig. 1: we are interested in reconstructing the formation's profile shown in Fig. 1(a), using records of the formation's response collected by sensors (geophones) dispersed over the formation's surface, when the formation is excited by active sources (Vibroseis equipment), also located on the surface. Given the arbitrary heterogeneity of the domain of interest, the problem is inherently three-dimensional. Herein, we describe the methodology by focusing on the two-dimensional counterpart of the original problem, as depicted in Fig. 1(b): we accept arbitrary heterogeneity within a two-dimensional slice, but presume that the properties remain unchanged along the third dimension, i.e., a plane strain problem. While, the problem, as defined, departs from the true physical three-dimensional case,[1] it still contains all the complexities associated with the three-dimensional problem. Fig. 1(c) represents the mathematical idealization of the two-dimensional slice shown in Fig. 1(b): the semi-infinite physical domain has been truncated to a finite one through the introduction of buffer layers (PMLs) meant to absorb the outgoing waves generated by the action of the active surface sources.

Thus, the site characterization problem reduces to the following inverse medium problem: find the Lamé parameters $\lambda(\boldsymbol{x})$ and $\mu(\boldsymbol{x})$ in Ω^{RD} using the recorded response at the sensor/receiver locations due to the (known) excitation applied at the source locations.

[1] The problem is still valid in the case of horizontal layers, or even in the case of inclined layers, or even in the case of arbitrary plane heterogeneity.

3. The inverse medium problem—theoretical aspects

Our objective is to find the spatially distributed elastic material properties of the probed site. We discuss a method that systematically finds the distribution of the material properties by minimizing the difference (misfit), in the least-squares sense, between the measured response recorded during a field experiment, and a computed response which results from numerically simulating the site's response under the same loads as those used during the field experiment. The computed response uses trial distributions of the material properties $\lambda(\boldsymbol{x}),\mu(\boldsymbol{x})$, which are continuously updated, until convergence (i.e., until the misfit is minimized). Since the numerically simulated response satisfies the governing partial differential equations (PDEs) that describe the physics of the problem, the process of finding the distributed material properties of the soil medium is forced to be constrained by the PDEs: the approach is often referred to as PDE-constrained optimization [15].

Inverse medium problems are notoriously ill-posed: at a minimum, they suffer from solution multiplicity, that is, different material distributions (potentially non-physical) could lead to a good agreement with the recorded data, i.e., be solutions to the misfit minimization problem. Thus, before undertaking the numerical solution of the inverse problem, the problem must be regularized, that is, it must be suitably transformed into a well-posed problem [17]. In the following sections, we discuss a robust algorithm for the numerical treatment of the inverse medium problem at hand. Most methods dealing with the solution of an inverse problem, including the present one, require the repeated solution of the forward problem, that is, the finding of the displacement field, under a known (or assumed) material distribution, known sources, and prescribed boundary and initial conditions. We, therefore, discuss first the forward problem and its numerical solution, which we use subsequently in tackling the inverse problem.

3.1. The forward problem

In the forward problem, we are concerned with the propagation of elastic waves in a semi-infinite, arbitrarily heterogeneous, elastic medium. The numerical simulation of such wave propagation problems, in which the physical domain extends to infinity, requires the truncation of the semi-infinite extent of the domain to yield a finite computational domain. This can be accomplished by placing perfectly-matched-layers (PMLs) at the truncation boundaries such that, ideally, when waves pass through the (theoretically) reflectionless interface, they get attenuated within the PML zone. The concept is schematically captured in Fig. 2.

To model the forward problem, we use a hybrid approach that has been recently developed (see, e.g. [8,9]), where the interior elastodynamic problem defined over the interior domain, henceforth labeled as *regular domain* and denoted by Ω^{RD}, is coupled with the physics governing the artificial wave attenuation within the PML domain, henceforth denoted by Ω^{PML}. We refer to [8,9] and references therein for the complete development of the method; here we repeat only the resulting coupled system of

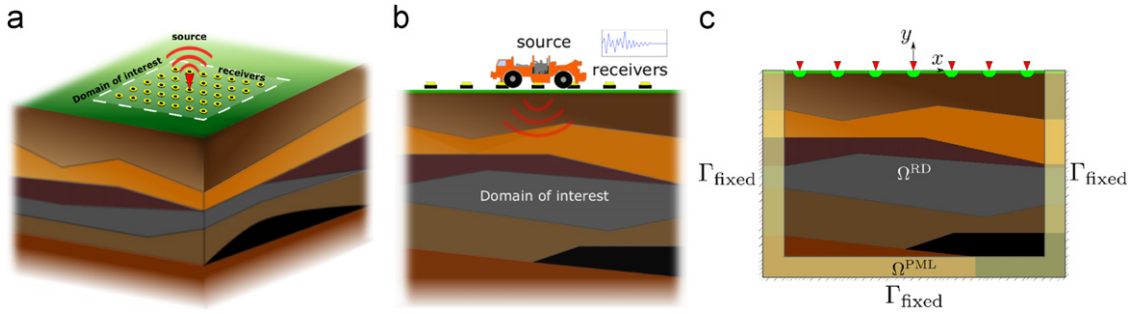

Fig. 1. Problem definition: (a) interrogation of a heterogeneous semi-infinite domain by an active source; (b) a 2D cross-section of the domain showing one source and multiple receivers; and (c) computational model truncated from the semi-infinite medium via the introduction of PMLs.

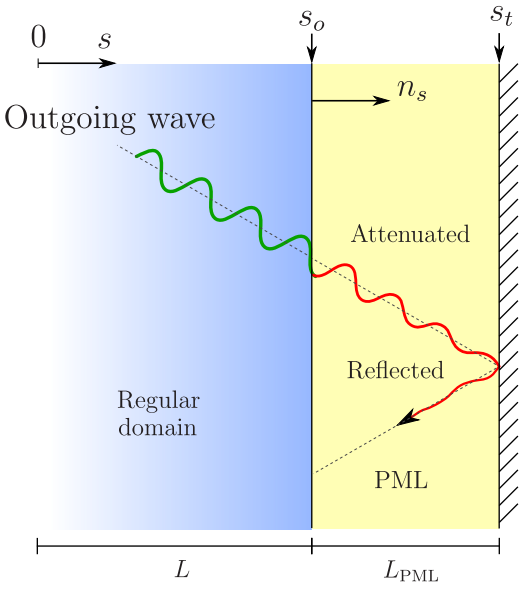

Fig. 2. Perfectly-matched-layer (PML) absorption concept.

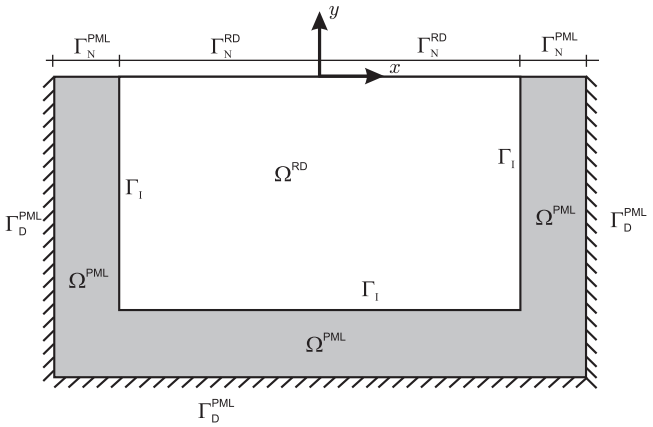

Fig. 3. A PML-truncated semi-infinite domain in two dimensions.

equations, by noting that the formulation is such that the interior domain is treated identically to a standard displacement-only elastodynamic problem, whereas the PML buffer is treated with a mixed formulation, where both displacements and stresses are unknown.

Accordingly, find $\boldsymbol{u}(\boldsymbol{x},t)$ in $\Omega^{\text{RD}} \cup \Omega^{\text{PML}}$, and $\boldsymbol{S}(\boldsymbol{x},t)$ in Ω^{PML} (see Fig. 3 for domain and boundary designations), where $\boldsymbol{u}$ and $\boldsymbol{S}$ reside in appropriate functional spaces and:

$$\text{div}\{\mu[\nabla\boldsymbol{u}+(\nabla\boldsymbol{u})^T]+\lambda(\text{div}\,\boldsymbol{u})\mathcal{I}\}+\boldsymbol{b}=\rho\ddot{\boldsymbol{u}} \quad \text{in } \Omega^{\text{RD}}\times J, \tag{1}$$

$$\text{div}\{\dot{\boldsymbol{S}}^T\tilde{\Lambda}_e+\boldsymbol{S}^T\tilde{\Lambda}_p\}=\rho(a\ddot{\boldsymbol{u}}+b\dot{\boldsymbol{u}}+c\boldsymbol{u}) \quad \text{in } \Omega^{\text{PML}}\times J, \tag{2}$$

$$\mathcal{D}[a\ddot{\boldsymbol{S}}+b\dot{\boldsymbol{S}}+c\boldsymbol{S}]=\frac{1}{2}[(\nabla\dot{\boldsymbol{u}})\tilde{\Lambda}_e+\tilde{\Lambda}_e(\nabla\dot{\boldsymbol{u}})^T+(\nabla\boldsymbol{u})\tilde{\Lambda}_p+\tilde{\Lambda}_p(\nabla\boldsymbol{u})^T] \quad \text{in } \Omega^{\text{PML}}\times J. \tag{3}$$

The system is initially at rest and subject to the following boundary and interface conditions:

$$\{\mu[\nabla\boldsymbol{u}+(\nabla\boldsymbol{u})^T]+\lambda(\text{div}\,\boldsymbol{u})\mathcal{I}\}\boldsymbol{n}=\boldsymbol{g}_n \quad \text{on } \Gamma_{\text{N}}^{\text{RD}}\times J, \tag{4}$$

$$\{\dot{\boldsymbol{S}}^T\tilde{\Lambda}_e+\boldsymbol{S}^T\tilde{\Lambda}_p\}\boldsymbol{n}=\boldsymbol{0} \quad \text{on } \Gamma_{\text{N}}^{\text{PML}}\times J, \tag{5}$$

$$\boldsymbol{u}=\boldsymbol{0} \quad \text{on } \Gamma_{\text{D}}^{\text{PML}}\times J, \tag{6}$$

$$\boldsymbol{u}^+=\boldsymbol{u}^- \quad \text{on } \Gamma_{\text{I}}\times J, \tag{7}$$

$$\{\mu[\nabla\boldsymbol{u}+(\nabla\boldsymbol{u})^T]+\lambda(\text{div}\,\boldsymbol{u})\mathcal{I}\}\boldsymbol{n}^+ +\{\dot{\boldsymbol{S}}^T\tilde{\Lambda}_e+\boldsymbol{S}^T\tilde{\Lambda}_p\}\boldsymbol{n}^-=\boldsymbol{0} \quad \text{on } \Gamma_{\text{I}}\times J. \tag{8}$$

In the above, $\boldsymbol{u}$ is the displacement vector, $\boldsymbol{b}$ is the vector of body forces, ρ denotes the mass density, $\dot{\boldsymbol{S}}$ represents the stress tensor, and a dot denotes differentiation with respect to time of the subtended variable. Moreover, $\tilde{\Lambda}_e$ and $\tilde{\Lambda}_p$ are the so-called stretch tensors corresponding to evanescent and propagating waves, respectively, which enforce dissipation of waves in Ω^{PML}, $\mathcal{D}[\cdot]$ is the fourth-order elasticity compliance tensor, and a, b, c are products of certain elements of the stretch tensors [8,9]. Moreover, $\boldsymbol{g}_n$ denotes prescribed surface tractions and $J=(0,T]$ denotes the time interval of interest. Eq. (1) is the governing PDE for the interior elastodynamic problem, whereas Eqs. (2) and (3) are the equilibrium, and combined kinematic and constitutive equations, respectively, for the PML zone. The last two equations allow one to maintain the temporal order of the interior problem (second), at the expense of introducing a mixed scheme for the PML zone.

We use a standard Galerkin finite element method for the spatial discretization of the interior elastodynamic domain, where the unknowns are the nodal displacements, and a non-classical mixed finite element technique for the unknowns in the PML domain (i.e., $\boldsymbol{u}$,$\boldsymbol{S}$). It can be shown [8,9] that the following system of ordinary differential equations results:

$$\boldsymbol{M}\ddot{\boldsymbol{d}}+\boldsymbol{C}\dot{\boldsymbol{d}}+\boldsymbol{K}\boldsymbol{d}=\boldsymbol{f}, \tag{9}$$

where $\boldsymbol{M}$, $\boldsymbol{C}$, $\boldsymbol{K}$ are system matrices, $\boldsymbol{d}$ is the vector of nodal unknowns comprising displacements in $\Omega^{\text{RD}}\cup\Omega^{\text{PML}}$, and stress components only in Ω^{PML}, and $\boldsymbol{f}$ is the vector of applied forces. Several methods can be used to integrate (9) in time; for example, application of the well-known family of Newmark methods

would require for the $n+1$-th time step to solve:

$$\hat{\boldsymbol{K}}\boldsymbol{d}^{n+1} = \boldsymbol{f}^{n+1} + \boldsymbol{M}(a_0\boldsymbol{d}^n + a_2\dot{\boldsymbol{d}}^n + a_3\ddot{\boldsymbol{d}}^n) + \boldsymbol{C}(a_1\boldsymbol{d}^n + a_4\dot{\boldsymbol{d}}^n + a_5\ddot{\boldsymbol{d}}^n), \tag{10}$$

where the effective stiffness is

$$\hat{\boldsymbol{K}} = a_0\boldsymbol{M} + a_1\boldsymbol{C} + \boldsymbol{K}, \tag{11}$$

and the velocity-like and acceleration-like updates are given by

$$\begin{aligned}\dot{\boldsymbol{d}}^{n+1} &= a_1(\boldsymbol{d}^{n+1} - \boldsymbol{d}^n) - a_4\dot{\boldsymbol{d}}^n - a_5\ddot{\boldsymbol{d}}^n,\\ \ddot{\boldsymbol{d}}^{n+1} &= a_0(\boldsymbol{d}^{n+1} - \boldsymbol{d}^n) - a_2\dot{\boldsymbol{d}}^n - a_3\ddot{\boldsymbol{d}}^n,\end{aligned} \tag{12}$$

in which a_0–a_5 are constants whose values depend on the choice of the particular Newmark method.[2] Given initial conditions $\boldsymbol{d}^0 = \boldsymbol{u}_0$, $\dot{\boldsymbol{d}}^0 = \boldsymbol{v}_0$, use of (10)–(12) allows the integration of the system of ordinary differential equations (ODEs). Alternatively, (10)–(12), supplemented by the initial conditions, can be cast in the following compact form:

$$\boldsymbol{Q}\hat{\boldsymbol{d}} = \hat{\boldsymbol{f}}, \tag{13}$$

where $\hat{\boldsymbol{d}} = [\boldsymbol{d}^0\ \dot{\boldsymbol{d}}^0\ \ddot{\boldsymbol{d}}^0\ \boldsymbol{d}^1\ \dot{\boldsymbol{d}}^1\ \ddot{\boldsymbol{d}}^1 \ldots \boldsymbol{d}^N\ \dot{\boldsymbol{d}}^N\ \ddot{\boldsymbol{d}}^N]^T$ corresponds to the space–time discretization of the unknown variables and their temporal derivatives (N is the number of time steps, and $\boldsymbol{d}^i$ are the spatial degrees of freedom at the i-th time step), and $\hat{\boldsymbol{f}} = [\boldsymbol{u}_0\ \boldsymbol{v}_0\ \boldsymbol{f}^0\ \boldsymbol{f}^1\ \boldsymbol{0}\ \boldsymbol{0} \ldots \boldsymbol{f}^N\ \boldsymbol{0}\ \boldsymbol{0}]^T$. The discrete forward operator $\boldsymbol{Q}$ is defined as:

$$\boldsymbol{Q} = \begin{bmatrix}
\boldsymbol{I} & \boldsymbol{0} & \boldsymbol{0} & \boldsymbol{0} & \boldsymbol{0} & \boldsymbol{0} & \cdots & \boldsymbol{0} & \boldsymbol{0} & \boldsymbol{0} & \boldsymbol{0} & \boldsymbol{0} & \boldsymbol{0}\\
\boldsymbol{0} & \boldsymbol{I} & \boldsymbol{0} & \boldsymbol{0} & \boldsymbol{0} & \boldsymbol{0} & \cdots & \boldsymbol{0} & \boldsymbol{0} & \boldsymbol{0} & \boldsymbol{0} & \boldsymbol{0} & \boldsymbol{0}\\
\boldsymbol{K} & \boldsymbol{C} & \boldsymbol{M} & \boldsymbol{0} & \boldsymbol{0} & \boldsymbol{0} & \cdots & \boldsymbol{0} & \boldsymbol{0} & \boldsymbol{0} & \boldsymbol{0} & \boldsymbol{0} & \boldsymbol{0}\\
\boldsymbol{L}_1 & \boldsymbol{L}_2 & \boldsymbol{L}_3 & \hat{\boldsymbol{K}} & \boldsymbol{0} & \boldsymbol{0} & \cdots & \boldsymbol{0} & \boldsymbol{0} & \boldsymbol{0} & \boldsymbol{0} & \boldsymbol{0} & \boldsymbol{0}\\
a_1\boldsymbol{I} & a_4\boldsymbol{I} & a_5\boldsymbol{I} & -a_1\boldsymbol{I} & \boldsymbol{I} & \boldsymbol{0} & \cdots & \boldsymbol{0} & \boldsymbol{0} & \boldsymbol{0} & \boldsymbol{0} & \boldsymbol{0} & \boldsymbol{0}\\
a_0\boldsymbol{I} & a_2\boldsymbol{I} & a_3\boldsymbol{I} & -a_0\boldsymbol{I} & \boldsymbol{0} & \boldsymbol{I} & \cdots & \boldsymbol{0} & \boldsymbol{0} & \boldsymbol{0} & \boldsymbol{0} & \boldsymbol{0} & \boldsymbol{0}\\
\vdots & \vdots & \vdots & \vdots & \vdots & \vdots & \ddots & \vdots & \vdots & \vdots & \vdots & \vdots & \vdots\\
\boldsymbol{0} & \boldsymbol{0} & \boldsymbol{0} & \boldsymbol{0} & \boldsymbol{0} & \boldsymbol{0} & \cdots & \boldsymbol{L}_1 & \boldsymbol{L}_2 & \boldsymbol{L}_3 & \hat{\boldsymbol{K}} & \boldsymbol{0} & \boldsymbol{0}\\
\boldsymbol{0} & \boldsymbol{0} & \boldsymbol{0} & \boldsymbol{0} & \boldsymbol{0} & \boldsymbol{0} & \cdots & a_1\boldsymbol{I} & a_4\boldsymbol{I} & a_5\boldsymbol{I} & -a_1\boldsymbol{I} & \boldsymbol{I} & \boldsymbol{0}\\
\boldsymbol{0} & \boldsymbol{0} & \boldsymbol{0} & \boldsymbol{0} & \boldsymbol{0} & \boldsymbol{0} & \cdots & a_0\boldsymbol{I} & a_2\boldsymbol{I} & a_3\boldsymbol{I} & -a_0\boldsymbol{I} & \boldsymbol{0} & \boldsymbol{I}
\end{bmatrix}, \tag{14}$$

where

$$\boldsymbol{L}_1 = -a_0\boldsymbol{M} - a_1\boldsymbol{C},$$

$$\boldsymbol{L}_2 = -a_2\boldsymbol{M} - a_4\boldsymbol{C},$$

$$\boldsymbol{L}_3 = -a_3\boldsymbol{M} - a_5\boldsymbol{C}.$$

We emphasize that (13) is precisely the Newmark algorithm written in a different form, which is better suited for the solution of the inverse medium problem at hand, as it will become apparent later. Notice that the first two rows of (14) recover the initial conditions, whereas the third row solves for $\ddot{\boldsymbol{d}}^0$. The fourth row solves for $\boldsymbol{d}^1$, and the fifth and sixth rows yield $\dot{\boldsymbol{d}}^1$ and $\ddot{\boldsymbol{d}}^1$, respectively. Finally, the last three rows, solve for $\boldsymbol{d}^N$, and update $\dot{\boldsymbol{d}}^N$, $\ddot{\boldsymbol{d}}^N$, respectively.

3.2. The inverse problem

Our goal is to find the distribution of the material properties $\lambda(\boldsymbol{x})$, $\mu(\boldsymbol{x})$ of the elastic soil medium, such that the misfit between the measured response at the receivers' locations and a computed response corresponding to a trial material profile is minimized. Mathematically, this is cast as a PDE-constrained optimization problem, in which we consider solving the following problem:

$$\min_{\lambda,\mu} \mathcal{J}(\lambda,\mu) := \frac{1}{2}\int_0^T \int_{\Gamma_m} (u-u_m)^2 b(x)\, ds(x)\, dt + \mathcal{R}(\lambda,\mu), \tag{15}$$

subject to the (continuous) forward problem governed by the initial- and boundary-value problem (1)–(8).

In the above, T is the total observation time, Γ_m denotes the part of the ground surface where the sensor response is recorded, u is the vertical component of the computed displacement, u_m corresponds to the measured vertical displacement component (obtained via sensor data processing), and $b(x)$ represents the point measurement operator defined by

$$b(x) = \sum_{j=1}^{N_r} \delta(x - x_j). \tag{16}$$

N_r denotes the total number of receivers and $\delta(x-x_j)$ is the Dirac delta function. Moreover, $\mathcal{R}(\lambda,\mu)$ is the regularization term that penalizes highly oscillatory material gradients and, thus, precludes spatially rapid material variations from becoming solutions to the inverse medium problem. We use the Tikhonov regularization scheme defined as

$$\mathcal{R}(\lambda,\mu) = \frac{R_\lambda}{2}\int_{\Omega^{\mathrm{RD}}} \nabla\lambda\cdot\nabla\lambda\, d\Omega^{\mathrm{RD}} + \frac{R_\mu}{2}\int_{\Omega^{\mathrm{RD}}} \nabla\mu\cdot\nabla\mu\, d\Omega^{\mathrm{RD}}, \tag{17}$$

where R_λ and R_μ are regularization parameters that control the amount of penalty imposed on the gradients of λ and μ.

One may use the (formal) Lagrangian approach [20], whereby the forward problem (1)–(8) is imposed via Lagrange multipliers (adjoint variables) to the functional (15). One then seeks a stationary point to the resulting Lagrangian functional, by forcing the first-order optimality conditions to vanish. The approach yields two initial-and-boundary value problems (the forward and the adjoint), and two time-independent boundary-value control problems, which, subsequently, all need to be discretized (in space and time), and solved at each inversion iteration [4,7]. Specifically, the forward problem is solved first, followed by the adjoint. Using next the state and adjoint solutions together with the control problems, the material gradients can be computed. The material gradients and the material distribution of the previous inversion iteration can then be used to update the material profile. The procedure is referred to as an *optimize-then-discretize* approach, since the optimality conditions are sought first in their continuous form, followed by a spatial discretization step, which, in turn, leads to the numerical solution. Such a procedure is discussed comprehensively in [4,7], where a gradient-based scheme is also used to iteratively update the material properties.

Alternatively, one may discretize the continuous constrained optimization problem (15) first, and then compute the corresponding *discrete* optimality conditions [2,15]. The procedure is referred to as a *discretize-then-optimize* approach [2]. In a way similar to the *optimize-then-discretize* approach, a gradient-based scheme may be used here as well, to iteratively update the material properties.

Herein, we opt for the *discretize-then-optimize* approach for the following reasons: the *optimize-then-discretize* approach yields an approximation of the gradient of the discrete functional (15), while the *discretize-then-optimize* approach yields the *exact* gradient of the discrete functional. Although both approaches involve approximation due to the discretization step, the *optimize-then-discretize* approach does not yield the exact gradient of either the continuous functional, or the discretized functional [2]. Therefore, the *optimize-then-discretize* approach may result in inconsistent gradients, which, in turn, may cause serious numerical difficulties; for

[2] For example, for a constant average acceleration scheme, $a_0 = 1/(\alpha\Delta t^2)$, $a_1 = \delta/(\alpha\Delta t)$, $a_2 = 1/(\alpha\Delta t)$, $a_3 = 1/(2\alpha) - 1$, $a_4 = \delta/\alpha - 1$, $a_5 = (\delta/2\alpha - 1)\Delta t$, where $\delta = 1/2$, $\alpha = 1/4$.

instance, a downhill direction as determined by the inconsistent gradient, may actually be an uphill direction of the functional. This may force the Armijo condition to be violated [13] and, eventually, force the optimizer to stop. The *discretize-then-optimize* approach, however, is more robust and does not suffer from such problems (see, e.g. [2, Chapter 4] for a comprehensive discussion and [15] for a systematic treatment and a detailed example).

3.2.1. Discrete optimality conditions

Discretization of the objective functional (15) in space and time yields

$$\min_{\boldsymbol{\lambda},\boldsymbol{\mu}} \boldsymbol{J}(\boldsymbol{\lambda},\boldsymbol{\mu}) \coloneqq \frac{1}{2}(\hat{\boldsymbol{d}}-\hat{\boldsymbol{d}}_m)^T\overline{\boldsymbol{B}}(\hat{\boldsymbol{d}}-\hat{\boldsymbol{d}}_m)+\frac{R_\lambda}{2}\boldsymbol{\lambda}^T\boldsymbol{R}\boldsymbol{\lambda}+\frac{R_\mu}{2}\boldsymbol{\mu}^T\boldsymbol{R}\,\boldsymbol{\mu}, \tag{18}$$

where $\hat{\boldsymbol{d}}$ satisfies the discrete forward problem (13). Here, $\boldsymbol{\lambda}$ and $\boldsymbol{\mu}$ are discrete material properties, $\hat{\boldsymbol{d}}_m$ are the discrete space–time measurement data, $\overline{\boldsymbol{B}}$ is the discretized (space–time) measurement operator,[3] and $\boldsymbol{R}$ is the matrix corresponding to the discretization scheme used for the regularization terms. The discrete Lagrangian corresponding to (18) becomes

$$\mathcal{L}(\hat{\boldsymbol{d}},\hat{\boldsymbol{p}},\boldsymbol{\lambda},\boldsymbol{\mu}) \coloneqq \boldsymbol{J}(\boldsymbol{\lambda},\boldsymbol{\mu})-\hat{\boldsymbol{p}}^T(\boldsymbol{Q}\hat{\boldsymbol{d}}-\hat{\boldsymbol{f}}), \tag{19}$$

where $\hat{\boldsymbol{p}}=[\boldsymbol{r}^0\ \boldsymbol{q}^0\ \boldsymbol{p}^0\ \boldsymbol{r}^1\ \boldsymbol{q}^1\ \boldsymbol{p}^1\ \cdots\ \boldsymbol{r}^N\ \boldsymbol{q}^N\ \boldsymbol{p}^N]^T$ is the *discrete* (space–time) Lagrange multiplier that enforces the *discrete* forward problem ($\boldsymbol{Q}\hat{\boldsymbol{d}}=\hat{\boldsymbol{f}}$) as a constraint.[4] The discrete optimality conditions for (19) are obtained by requiring that the derivatives of the Lagrangian with respect to each of the variables vanish. Taking the derivative with respect to the Lagrange multiplier $\hat{\boldsymbol{p}}$ recovers the discrete forward problem (13), which in this context, we refer to as the discrete state equation:

$$\mathcal{L}_{\hat{\boldsymbol{p}}}(\hat{\boldsymbol{d}},\hat{\boldsymbol{p}},\boldsymbol{\lambda},\boldsymbol{\mu}) = -\boldsymbol{Q}\hat{\boldsymbol{d}}+\hat{\boldsymbol{f}}=\boldsymbol{0}. \tag{20}$$

We remark that Eq. (20) has the structure discussed earlier in Section 3.1. The discrete adjoint equation is obtained by requiring that the derivative of the discrete Lagrangian with respect to $\hat{\boldsymbol{d}}$ vanish, that is

$$\mathcal{L}_{\hat{\boldsymbol{d}}}(\hat{\boldsymbol{d}},\hat{\boldsymbol{p}},\boldsymbol{\lambda},\boldsymbol{\mu}) = -\boldsymbol{Q}^T\hat{\boldsymbol{p}}+\boldsymbol{B}(\hat{\boldsymbol{d}}-\hat{\boldsymbol{d}}_m)=\boldsymbol{0}. \tag{21}$$

We remark that (21) involves the transpose of $\boldsymbol{Q}$, and hence, (21) is solved by marching backwards in time. For example, from the last two rows of (21), we obtain the final conditions

$$\boldsymbol{p}^N=\boldsymbol{0}, \tag{22}$$

$$\boldsymbol{q}^N=\boldsymbol{0}, \tag{23}$$

respectively; and the third row from the bottom yields

$$\hat{\boldsymbol{K}}^T\boldsymbol{r}^N=\Delta t\boldsymbol{B}(\boldsymbol{d}^N-\boldsymbol{d}_m^N)+a_1\boldsymbol{q}^N+a_0\boldsymbol{p}^N, \tag{24}$$

which can be solved for $\boldsymbol{r}^N$. For time steps $n=N, N-1,\ldots,2$, we deduce the following algorithm:

$$\begin{aligned}\text{update}: \quad \boldsymbol{p}^{n-1} &= (a_3\boldsymbol{M}^T+a_5\boldsymbol{C}^T)\boldsymbol{r}^n-a_5\boldsymbol{q}^n-a_3\boldsymbol{p}^n,\\ \boldsymbol{q}^{n-1} &= (a_2\boldsymbol{M}^T+a_4\boldsymbol{C}^T)\boldsymbol{r}^n-a_4\boldsymbol{q}^n-a_2\boldsymbol{p}^n,\end{aligned} \tag{25}$$

$$\begin{aligned}\text{solve}: \quad \hat{\boldsymbol{K}}^T\boldsymbol{r}^{n-1} &= \Delta t\boldsymbol{B}(\boldsymbol{d}^{n-1}-\boldsymbol{d}_m^{n-1})+a_1\boldsymbol{q}^{n-1}+a_0\boldsymbol{p}^{n-1}\\ &\quad +(a_0\boldsymbol{M}^T+a_1\boldsymbol{C}^T)\boldsymbol{r}^n-a_1\boldsymbol{q}^n-a_0\boldsymbol{p}^n.\end{aligned} \tag{26}$$

Notice that contrary to the conventional application of Newmark's method, here we first update, and then solve. Finally, the first three rows of (21) result in the following equations:

$$\text{solve}: \quad \boldsymbol{M}^T\boldsymbol{p}^0=(a_3\boldsymbol{M}^T+a_5\boldsymbol{C}^T)\boldsymbol{r}^1-a_5\boldsymbol{q}^1-a_3\boldsymbol{p}^1 \tag{27}$$

$$\begin{aligned}\text{update}: \quad \boldsymbol{q}^0 &= -\boldsymbol{C}^T\boldsymbol{p}^0+(a_2\boldsymbol{M}^T+a_4\boldsymbol{C}^T)\boldsymbol{r}^1-a_4\boldsymbol{q}^1-a_2\boldsymbol{p}^1,\\ \boldsymbol{r}^0 &= -\boldsymbol{K}^T\boldsymbol{p}^0+(a_0\boldsymbol{M}^T+a_1\boldsymbol{C}^T)\boldsymbol{r}^1-a_1\boldsymbol{q}^1-a_0\boldsymbol{p}^1+\Delta t\boldsymbol{B}(\boldsymbol{d}^0-\boldsymbol{d}_m^0).\end{aligned} \tag{28}$$

The third discrete optimality condition is obtained by setting the derivative of (19) with respect to $\boldsymbol{\lambda}$ and $\boldsymbol{\mu}$ to zero. That is

$$\mathcal{L}_{\boldsymbol{\lambda}}(\hat{\boldsymbol{d}},\hat{\boldsymbol{p}},\boldsymbol{\lambda},\boldsymbol{\mu}) = R_\lambda\boldsymbol{R}\,\boldsymbol{\lambda}-\hat{\boldsymbol{p}}^T\frac{\partial\boldsymbol{Q}}{\partial\boldsymbol{\lambda}}\hat{\boldsymbol{d}}=\boldsymbol{0}, \tag{29}$$

$$\mathcal{L}_{\boldsymbol{\mu}}(\hat{\boldsymbol{d}},\hat{\boldsymbol{p}},\boldsymbol{\lambda},\boldsymbol{\mu}) = R_\mu\boldsymbol{R}\,\boldsymbol{\mu}-\hat{\boldsymbol{p}}^T\frac{\partial\boldsymbol{Q}}{\partial\boldsymbol{\mu}}\hat{\boldsymbol{d}}=\boldsymbol{0}, \tag{30}$$

where the terms $\partial\boldsymbol{Q}/\partial\boldsymbol{\lambda}$ and $\partial\boldsymbol{Q}/\partial\boldsymbol{\mu}$ can be computed in a straightforward manner (the details are given in the Appendix).

Satisfaction of (18) requires simultaneous solution of equations (20), (21), (29) and (30), which is possible in principle, but rather expensive in practice. Alternatively, an iterative procedure may be used such that the discrete material properties are updated according to a gradient-based scheme. The scheme is outlined in [7], and we briefly discuss it here for completeness.

3.2.2. Gradient-based optimization algorithm

In gradient-based algorithms, the material properties are updated iteratively using the gradient of the discrete functional (18) with respect to $\boldsymbol{\lambda}$ and $\boldsymbol{\mu}$, until the objective functional is minimized. After initializing the material properties, at every iteration (say k), we solve the discrete state equation (20) to obtain $\hat{\boldsymbol{d}}_k$. With the misfit known at iteration k, we use next the discrete adjoint equation (21) to solve for $\hat{\boldsymbol{p}}_k$. With $\hat{\boldsymbol{d}}_k$ and $\hat{\boldsymbol{p}}_k$ known, the gradients can be computed from

$$\tilde{\boldsymbol{M}}\boldsymbol{g}_k^{\lambda} \coloneqq \nabla_{\boldsymbol{\lambda}}\boldsymbol{J}(\boldsymbol{\lambda}_k,\boldsymbol{\mu}_k) = \mathcal{L}_{\boldsymbol{\lambda}}(\hat{\boldsymbol{d}}_k,\hat{\boldsymbol{p}}_k,\boldsymbol{\lambda}_k,\boldsymbol{\mu}_k), \tag{31}$$

$$\tilde{\boldsymbol{M}}\boldsymbol{g}_k^{\boldsymbol{\mu}} \coloneqq \nabla_{\boldsymbol{\mu}}\boldsymbol{J}(\boldsymbol{\lambda}_k,\boldsymbol{\mu}_k) = \mathcal{L}_{\boldsymbol{\mu}}(\hat{\boldsymbol{d}}_k,\hat{\boldsymbol{p}}_k,\boldsymbol{\lambda}_k,\boldsymbol{\mu}_k), \tag{32}$$

where the second equality in each of (31) and (32) is due to the satisfaction of the discrete state problem [20]. Furthermore, at a stationary point of (18), the gradients are zero, as suggested by the third discrete optimality condition (29) and (30). In (31) and (32), $\tilde{\boldsymbol{M}}$ is given as

$$\tilde{\boldsymbol{M}} = \int_{\Omega^{\mathrm{RD}}}\boldsymbol{\chi}\boldsymbol{\chi}^T\,d\Omega^{\mathrm{RD}}, \tag{33}$$

where $\boldsymbol{\chi}$ are material interpolants (see Appendix). A search algorithm may now be used to update the nodal material properties

$$\boldsymbol{\lambda}_{k+1}=\boldsymbol{\lambda}_k+\alpha_k^{\lambda}\boldsymbol{s}_k^{\lambda}, \tag{34}$$

$$\boldsymbol{\mu}_{k+1}=\boldsymbol{\mu}_k+\alpha_k^{\mu}\boldsymbol{s}_k^{\mu}, \tag{35}$$

where α_k^{λ}, α_k^{μ} are step lengths, and $\boldsymbol{s}_k^{\lambda}$, $\boldsymbol{s}_k^{\mu}$ are the search directions for $\boldsymbol{\lambda}$ and $\boldsymbol{\mu}$, respectively. Search directions may be determined simply by choosing the direction of steepest descent (i.e., $\boldsymbol{s}_k^{(\cdot)}=-\boldsymbol{g}_k^{(\cdot)}$) or, more suitably, by using a conjugate gradient method as was done for the results discussed herein. Moreover, a line search algorithm for determining the step length $\alpha_k^{(\cdot)}$ is also required [7].

4. Inversion results using synthetic data

We discuss next numerical experiments involving the characterization of target sites for which we use synthetic data. Since the primary focus in this paper is on field data rather than on

[3] $\overline{\boldsymbol{B}}$ is a block diagonal matrix with $\Delta t\boldsymbol{B}$ on the diagonal; Δt denotes the time step, and $\boldsymbol{B}$ is a square matrix that is zero everywhere except on the diagonals that correspond to a degree of freedom for which measured data are available.

[4] Though not necessary, $\boldsymbol{q}^i$ can be thought of as $\dot{\boldsymbol{p}}^i$, and $\boldsymbol{r}^i$ as $\ddot{\boldsymbol{p}}^i$ at the i-th time step.

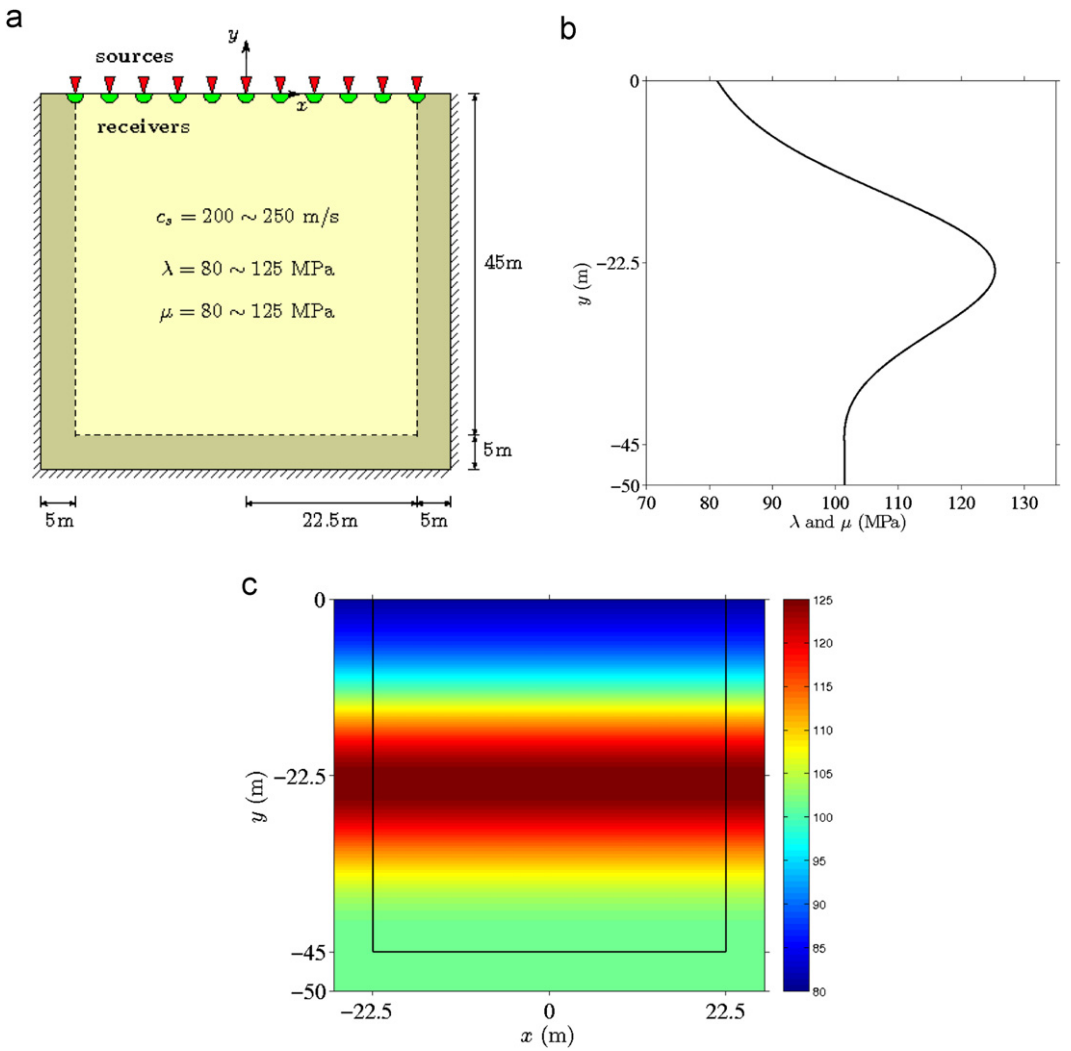

Fig. 4. Site characterization for an idealized target—smoothly-varying material profile ($\lambda = \mu$): (a) geometry, (b) typical cross-section, and (c) target Lamé parameters λ and μ.

synthetic data cases, we discuss only a subset of numerical results with synthetic data. The first example involves a domain with a smoothly varying (in depth) profile (Fig. 4(b)), i.e., a domain comprising an infinite number of horizontal layers. The originally semi-infinite domain has been reduced through truncation to a 45 m × 45 m computational domain, surrounded on its sides and bottom by a 5 m-thick PML, as shown in Fig. 4(a). Sources and receivers occupy the entire ground surface (at grid points). The inversion process was started with a homogeneous initial guess that had both λ and μ set to 80 MPa. We used a Gaussian pulse with a maximum frequency of 40 Hz to probe the domain. The results of the inversion are shown in Fig. 5 where, as it can be seen, both Lamé parameters are quite satisfactorily recovered.

A second example involves a layered medium with $\lambda(x_2) = \mu(x_2) = 320$, 500, and 720 MPa from top to bottom (see Fig. 6 for the detailed layering geometry). An elliptic inclusion of 720 MPa ($\lambda = \mu$) is also embedded in an effort to introduce arbitrary heterogeneity.[5] Here, we used a source-frequency continuation scheme with four distinct Gaussian pulses ($f_{\max} = 10$, 40, 80, and 120 Hz), to probe the domain (again sources and receivers are spread over the entire ground surface). We initiated the inversion process with a homogeneous initial guess that had λ and μ set to 310 MPa. Fig. 7 depicts the spatial distribution of the compressional and shear wave velocity profiles computed from the reconstructed λ and μ. Both velocity profiles seem to have been recovered satisfactorily.

5. The field experiment—design considerations

In this section, we discuss the design of a field experiment that will provide us with field-measured data, which can then be used to exercise the two-dimensional inversion codes we developed based on the preceding theory. To this end, we attempt to generate plane strain conditions in the field, so that we then attempt to invert for the properties of a two-dimensional site slice (Fig. 8(c)). Since the loads we can impart on the ground surface are really three-dimensional, plane strain conditions would require loading along densely populated lines (Fig. 8(a)) to emulate theoretical line loads. In this section, we discuss how this can be accomplished in a practical manner. Naturally, to replicate plane strain conditions in the field, the loading is only one of the difficulties: a key assumption we make here is that there is lateral material homogeneity, that is, the site slice may be, in plane, arbitrarily heterogeneous, but the properties do not change

[5] The target Lamé parameters are set equal to each other without loss of generality. The inversion is performed simultaneously for both parameters.

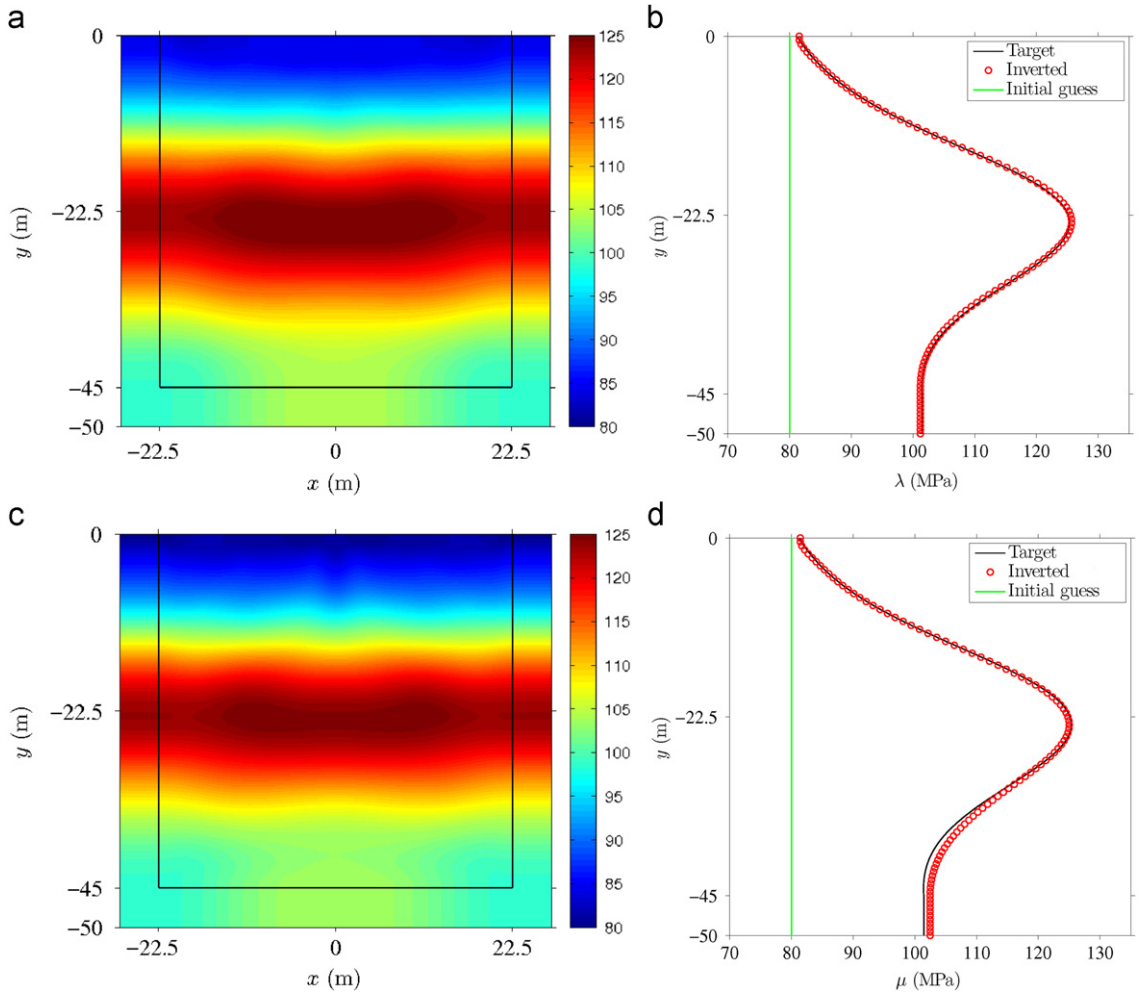

Fig. 5. Simultaneous inversion for the Lamé parameters: (a) reconstructed λ, (b) λ at the $x_1 = 0$ m cross-section, (c) Reconstructed μ and (d) μ at the $x_1 = 0$ m cross-section.

along the direction perpendicular to the slice. While restrictive, the assumption is realistic for layered sites, is a significant improvement upon pervasive one-dimensional assumptions of other methodologies, and, due to prior characterizations, it was a reasonable assumption to make for the specific field experiment site.

With these assumptions in mind, the question becomes: how can a line load be approximated by a sequence of loads in the field, which may resemble point loads, and are suitably spaced along straight lines whose extent remains finite (line loads are infinite in extent)? The question is depicted in Fig. 8. Therefore, we are interested in arriving at an estimate of the spacing between the loads, and an estimate of the finite extent of the line of loads. We focus next on these two questions of spatial load distribution, but, in parallel, we also address the temporal variability of the load signal. We sketch the process on the basis of a homogeneous halfspace by drawing on classical solutions; site-specific conditions will also have an effect on load spacing and load extent, but when the design is based on the minimum expected wavelength, then the design is conservative.

Our methodology is based on the time-domain point-load analytical solutions in two-dimensional and three-dimensional space, that is, Lamb's problem and the Pekeris–Mooney's problem, respectively [5]. We use these solutions to derive the response of a two-dimensional or three-dimensional soil domain due to (temporally) arbitrary loads. In this way, the problem of designing the experiment reduces to a parametric study. We study first the effect of truncating the line load from extending to infinity by finding a

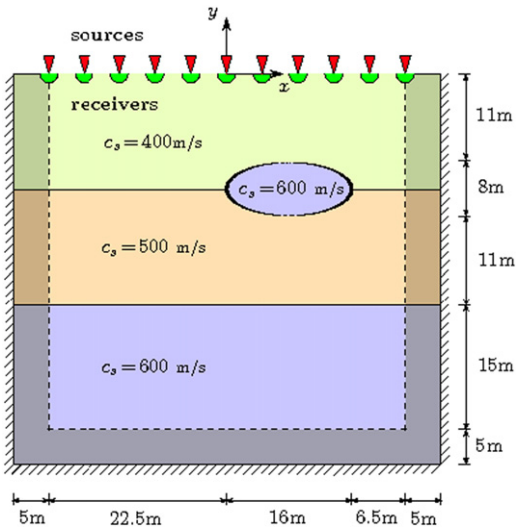

Fig. 6. A PML-truncated layered semi-infinite domain with an elliptic inclusion.

suitable truncation length. Then, we replace the truncated load line with equivalent point sources and determine the appropriate spacing between them. Fig. 8 displays schematically this objective. Finally, we comment on designing signals that are appropriate for

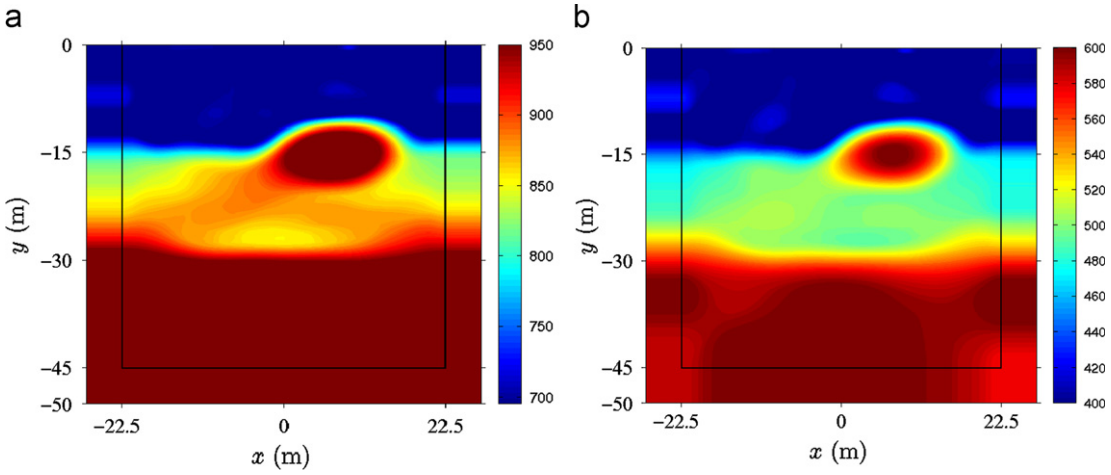

Fig. 7. Velocities computed from the reconstructed Lamé parameters: (a) c_p (m/s) and (b) c_s (m/s).

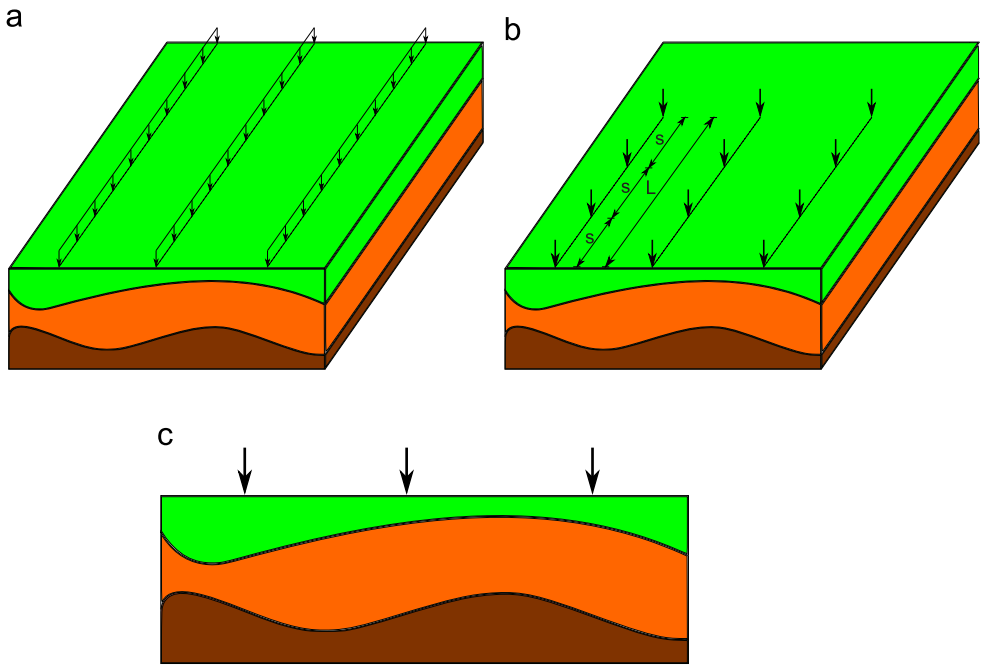

Fig. 8. Approximation of a 3D halfspace problem by a 2D halfplane problem. (a) 3D heterogeneous halfspace subjected to a series of line loads extending to infinity; heterogeneity is in plane only. (b) 3D heterogeneous halfspace subjected to a finite number of point sources spaced apart by s, arranged along lines of L total length. (c) Equivalent 2D halfplane subjected to concentrated sources.

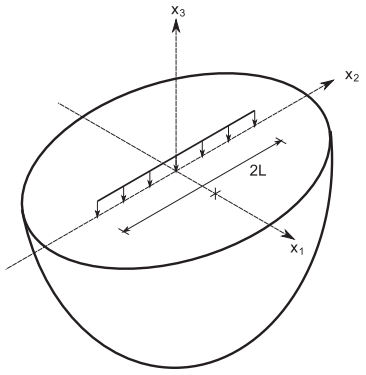

Fig. 9. Line load with a finite length.

Table 1
Material properties used in load verification examples.

P-wave velocity	$c_p=346.4$ m/s
S-wave velocity	$c_s=200.0$ m/s
R-wave velocity	$c_R=183.9$ m/s
Poisson's ratio	$v=0.25$

probing geotechnical sites and also discuss theoretical and practical issues that arise in such field experiments.

5.1. Line load truncation and spacing requirements

An impulsive in-plane point load is applied on the surface of a halfplane and the resulting displacements are sought. This plane

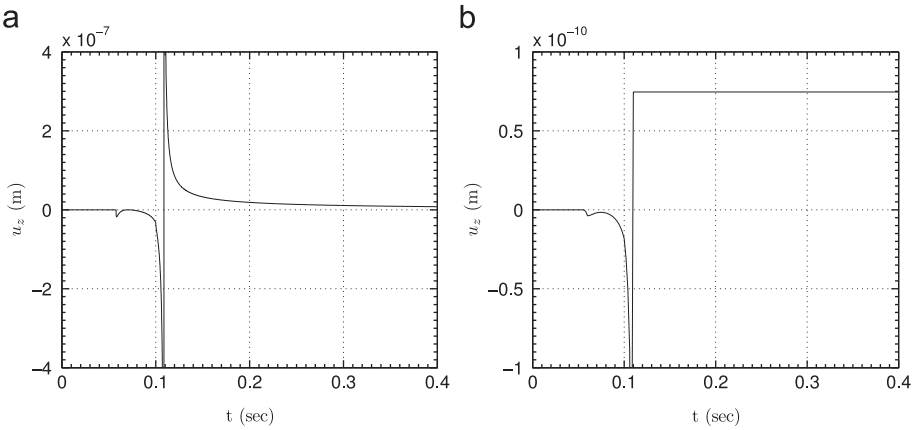

Fig. 10. 2D and 3D Green's functions: (a) Lamb's solution and (b) Pekeris–Mooney's solution.

strain problem is equivalent to an infinite line load applied on the surface of a halfspace. We denote the vertical displacement of a point $(x_1,0)$ at time t by $G^{2D}(x_1,t)$, where G^{2D} stands for Green's function, and the impulse load acts at the origin. The temporal dependence of the load can be described via the Dirac-delta function: exploiting superposition, we obtain the response due to any arbitrary time signal, denoted by $f^{2D}(t)$, via the following convolution integral:

$$u^{2D}(x_1,t)=\int_0^t f^{2D}(\tau)G^{2D}(x_1,t-\tau)\,d\tau. \tag{36}$$

The above relation allows us to compute the response of a halfplane subjected to any temporally arbitrary vertical force that acts on its surface. Special care must be taken when computing the integral since it has a singularity due to the arrival of the Rayleigh wave. Therefore, the integral should be interpreted in the Cauchy principal value sense. Details of Green's function $G^{2D}(x_1,t)$ can be found in [5].

A vertical point source that varies as a step function in time is applied on the surface of a halfspace. The vertical displacement of a point $(x_1,x_2,0)$ at time t is denoted by $G^{3D}(x_1,x_2,t)$, and the load acts at the origin. Details of the Green's function G^{3D} are given in the Appendix. The time signal can be described via a Heaviside function. However, we are interested in obtaining the response due to any arbitrary load, not only those with a simple step-like signature. Hence, our first attempt in making this problem fit into our needs, is to represent any arbitrary load $f^{3D}(t)$ as a summation of Heaviside functions and denote this approximation by $f_n^{3D}(t)$. Indeed, given $n+1$ pairs $\{t_i,f_i=f^{3D}(t_i)\}$, $i=0,1,\ldots,n$, we have

$$f_n^{3D}(t)=\frac{1}{2}(f_0+f_1)(H_0-H_1)+\tfrac{1}{2}(f_1+f_2)(H_1-H_2)+\cdots +\frac{1}{2}(f_{n-1}+f_n)(H_{n-1}-H_n), \tag{37}$$

where we used $H_i\equiv H(t-t_i)$ for notational simplicity; t_i indicates time value at node i. Re-arranging the above relation yields the following more convenient form:

$$f_n^{3D}(t)=\sum_{i=0}^{n} h_i H(t-t_i), \tag{38}$$

where

$$h_i=\begin{cases}\frac{1}{2}(f_0+f_1) & \text{for } i=0,\\ -\frac{1}{2}(f_{n-1}+f_n) & \text{for } i=n,\\ \frac{1}{2}(f_{i+1}-f_{i-1}) & \text{otherwise.}\end{cases} \tag{39}$$

Next, we consider a uniform distribution of point sources with a Heaviside time signature along a line of finite length. Without loss of generality, we assume that the sources are positioned symmetrically about the origin and occupy a total length of $2L$ along the x_2-axis (see Fig. 9). The response of the halfspace to this distribution, at any arbitrary point on the surface along the x_1-axis at time t is denoted by $G^{2L}(x_1,t)$, and is obtained by the following relation:

$$G^{2L}(x_1,t)=\int_{-L}^{L} G^{3D}(x_1,x_2,t)\,dx_2, \tag{40}$$

where $G^{2L}(x_1,t)$ may be interpreted as Green's function of a truncated line load. We expect that, at the limit as $L\to\infty$, G^{2L} reduces to the solution of the corresponding plane strain problem in the x_1-x_3 plane. Analytical expressions for the integral exist and are discussed in detail in the Appendix. Finally, combining (38) and (40), we obtain the response of the halfspace due to any arbitrary in time but uniform in space load, with a total length of $2L$ as

$$u^{2L}(x_1,t)=\sum_{i=0}^{n} h_i G^{2L}(x_1,t-t_i). \tag{41}$$

Relation (41) can be compared against (36) to find the appropriate truncation length L.

Once L is determined, the next step is to replace the continuous line load, with point sources. This is readily available by combining $G^{3D}(x_1,x_2,t)$ with (38): if we consider $2m+1$ point sources, symmetrically positioned along the x_2-axis, and spaced s distance apart such that $s=L/m$, the response of the halfspace at a point along the x_1-axis, may be obtained via:

$$u_s^{2L}(x_1,t)=\sum_{i=0}^{n} sh_i G^{3D}(x_1,0,t-t_i)+2\sum_{j=1}^{m}\sum_{i=0}^{n} sh_i G^{3D}(x_1,js,t-t_i). \tag{42}$$

Relations (36) and (42) can be compared against each other to determine the appropriate spacing between point sources.

5.2. Verification

We consider two numerical experiments to verify the derivation and numerical implementation of (36) and (41). We consider the material properties summarized in Table 1 for the homogeneous, isotropic elastic medium under consideration (notice not all of these properties are independent).

Lamb and Pekeris–Mooney's Green's functions are shown in Fig. 10 where the observer is located at $x_1=20$ m away from the source.

The P-wave arrives first, followed by the arrival of the S-wave with a change in slope. The Rayleigh surface wave comes next, and results in an infinite displacement that corresponds to the singularity of the associated Green's function. Moreover, in the

case of the Pekeris–Mooney's problem, the steady-state response that follows after the Rayleigh singularity corresponds to the Boussinesq's solution to a static load, acting on a halfspace.

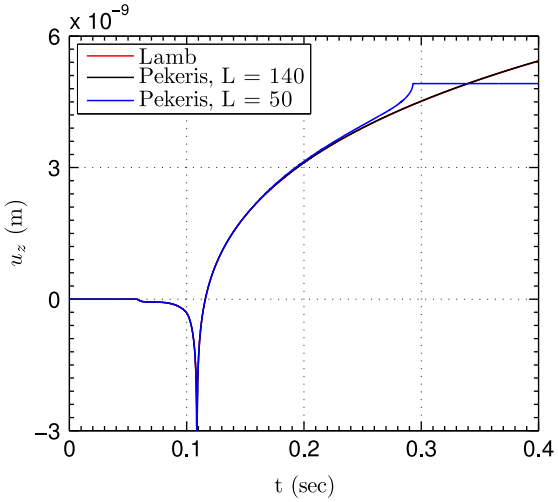

Fig. 11. Comparison of 2D and 3D systems due to a suddenly applied load.

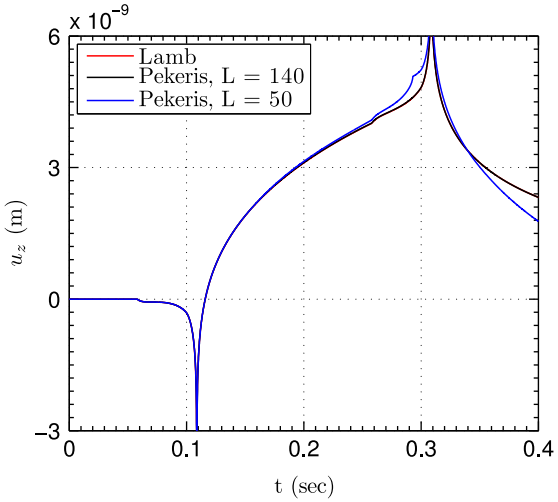

Fig. 12. Comparison of 2D and 3D systems due to a rectangular pulse load.

Example 1. We consider a suddenly applied vertical load, with $f(t)=H(t)$. Then, in (36) we have $f^{2D}(t)=1$ and only one term of the series in (41) is sufficient, namely $h_0=1$, while $t_0=0$.

Considering the value of the P-wave velocity, if we desire to plot the response up to 0.4 s, the farthest point from the observer that contributes to the response is located 140 m away. This means that taking $L=140$ m should yield identical results when comparing (36) and (41). Indeed, this is the case as shown in Fig. 11. We also include the case of $L=50$ m, which clearly deviates from the exact and the $L=140$ m case. The deviation begins at $t\approx 0.14$ s, and is more pronounced at around $t=0.27$ s. These times correspond to the arrival of the P- and S-wave from the farthest loaded point (i.e., $x_2=50$ m), respectively. Finally, the response reached a steady-state value at around 0.29 s, which corresponds to the arrival of the Rayleigh wave from the farthest point. Therefore, we conclude that for this example, the discrepancy can mostly be attributed to the arrival of Rayleigh waves from the farthest point followed by the final arrival of the S-wave, whereas the P-wave has a negligible effect in this regard.

Example 2. We consider a rectangular pulse such that $f(t)=H(t)-H(t-0.2)$. Hence, two terms of the series in (41) are sufficient, i.e. $h_0=1$ and $h_1=-1$, while $t_0=0$ and $t_1=0.2$. We compare (36) and (41) for the same L values and observer location as in the previous example.

Results are displayed in Fig. 12. The agreement is excellent between the two relations when L is sufficiently large; the discrepancies result from choosing small values for L. We emphasize that the two singularities in the plot correspond to the particular character of the load which initiates and terminates sharply.

5.3. Signal design

In this section, we comment on the main features that must be considered in designing signals for site characterization applications

Table 2
Chirp signals used in the field experiment.

Chirp name	f_0	k	f_{min}	f_{max}
C-3-8	3	1	3	8
C-8-20	8	2.4	8	20
C-20-25	20	1	20	25
C-25-35	25	2	25	35

Fig. 13. NEES@UTexas Liquidator Vibroseis.

based on full waveform-based inversion. For the field experiment, we conducted we used the Vibroseis trucks of the NEES@UTexas site (National Science Foundation, Network for Earthquake Engineering Simulation). In particular, we used T-Rex (tri-axial Vibroseis), and Liquidator (low-frequency Vibroseis) (Fig. 13). T-Rex can apply vertical loads with a maximum force amplitude of 267 kN within a frequency range from 12 Hz to about 180 Hz. It can also be used for applying loads outside this frequency range with a lower force amplitude. Liquidator is, however, more widely used when low frequency loading is desired. Liquidator is capable of applying loads within a frequency range of 1.3–75 Hz, with a peak force amplitude of 89 kN. Thus, from a practical standpoint, the desired frequency content and amplitude of loading should be restricted within the aforementioned ranges. To record the motion on the ground surface, we used 1 Hz geophones.

Our forward and inverse simulators are based on finite element discretization of the geotechnical site of interest. High frequency probing waves require a fine mesh resolution, and, thus, result in an increased computational cost. Therefore, they should be avoided whenever possible, unless fine features of the formation are of interest. Signals with long time duration require a longer observation period, thus also resulting in increased computation time, and increased storage requirements (the solution history must be stored at every time step for inverse problems [2]). Therefore, the time duration of a signal should be only long enough to effectively probe the depth of interest.

We favor signals that probe the geotechnical site of interest more effectively. Typically, these are signals that encompass a range of frequencies rather than containing only few isolated frequencies. The most commonly used class of these signals

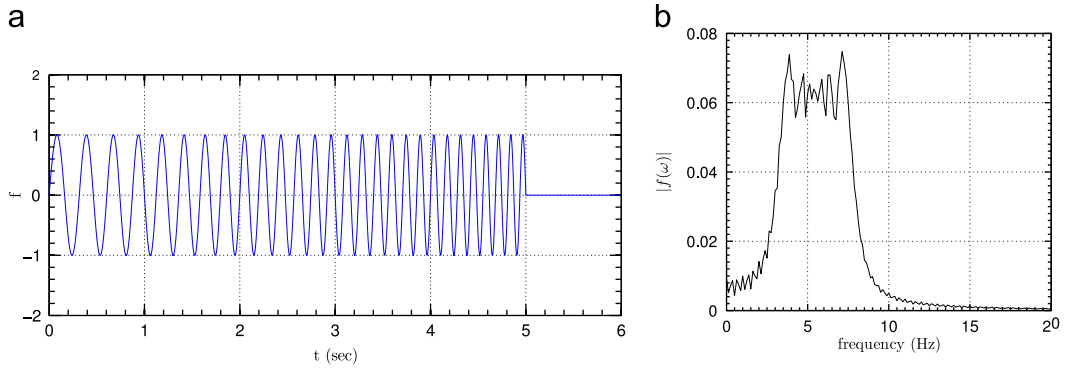

Fig. 14. Chirp with dominant frequencies between 3 Hz and 8 Hz: (a) signal time-history and (b) Fourier spectrum.

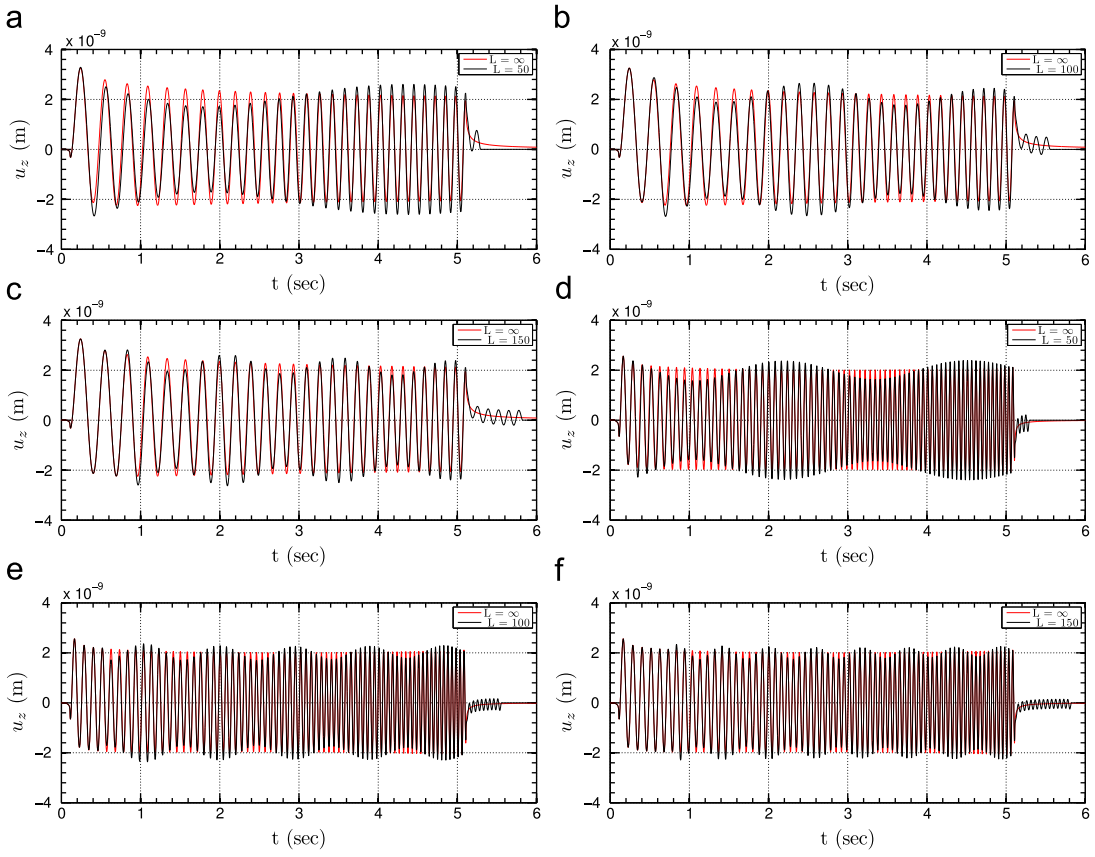

Fig. 15. Line load truncation effect for different chirps: (a) $L=50$, $L=\infty$ for Chirp C-3-8; (b) $L=100$, $L=\infty$ for Chirp C-3-8; (c) $L=150$, $L=\infty$ for Chirp C-3-8; (d) $L=50$, $L=\infty$ for Chirp C-8-20; (e) $L=100$, $L=\infty$ for Chirp C-8-20; and (f) $L=150$, $L=\infty$ for Chirp C-8-20.

are chirps, and have shown their effectiveness in radar and geophysical applications. In this experiment, we use linear chirps of the form

$$f(t)=\sin\left(2\pi\left(f_0+\frac{kt}{2}\right)t\right),$$

where f_0 is the starting frequency, and k is the chirp rate. With these two parameters, we can design a signal that has a desired frequency range. The starting frequency may be limited according to the geophone's resonant frequency, and k is determined according to the upper bound of the desired frequency range and total time duration of the signal. We consider four different chirp-type signals with an active and total time duration of 5 s and 8 s, respectively, which in total, span a frequency range of 3–35 Hz. These are summarized in Table 2. The dominant frequencies of the chirp lie between f_{min} and f_{max}. For example, Fig. 14 shows chirp's C-3-8 time dependence and frequency spectrum, where the strong components are clearly concentrated in the range of 3–8 Hz. Finally, we remark that the signals in Table 2 cannot be applied on the ground surface by either T-Rex or Liquidator in their exact form. Indeed, the equipment is only able to exert a load that is "close" to the design load. Therefore, it becomes necessary to measure the exact applied load due to its significance in the inversion process. This is done by installing accelerometers on the baseplate and reaction mass of the Vibroseis equipment. The actual applied load can be obtained by adding the products of the baseplate mass and the reaction mass by their corresponding measured accelerations.

5.4. Parametric studies

In the preceding sections, we developed all the tools we need for the parametric studies that we carry out in this section. We use (38) to represent signals considered in Table 2 with their corresponding Heaviside expansion. We then use (41) with a sufficiently large value for L to obtain the response of a 2D system and use it as a benchmark to find smaller values for L that yield comparable results. Once an appropriate value for L is determined, (42) can be used to find out a suitable spacing between equivalent point sources.

In order to determine the appropriate length for the line load, we consider three representative values for L: 50 m, 100 m, and 150 m. We compare the response of these cases against the benchmark solution (large L value) due to the four loads considered in Table 2. This leads to 12 numerical experiments which provide insight on how the frequency content of the load may play a role in selecting L.

Results for the first two chirps of Table 2 are shown in Fig. 15. Each plot depicts two curves, one obtained using the infinite line load length, and the other obtained using a finite value for L. The agreement between the two curves is remarkable for all cases, considering that the observation period is 6 s and the line load has a relatively short length. We note that for an exact match up to 6 s, a line load of length $L=2100$ m is required. We also observe that larger values of L yield better results, which is indeed intuitive. Results of the last two chirps of Table 2 also follow a similar trend. We choose the case of $L=100$ m for further investigations in subsequent sections.

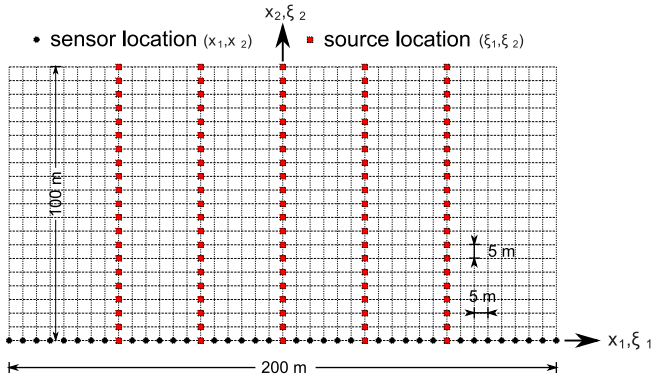

Fig. 17. The field experiment layout.

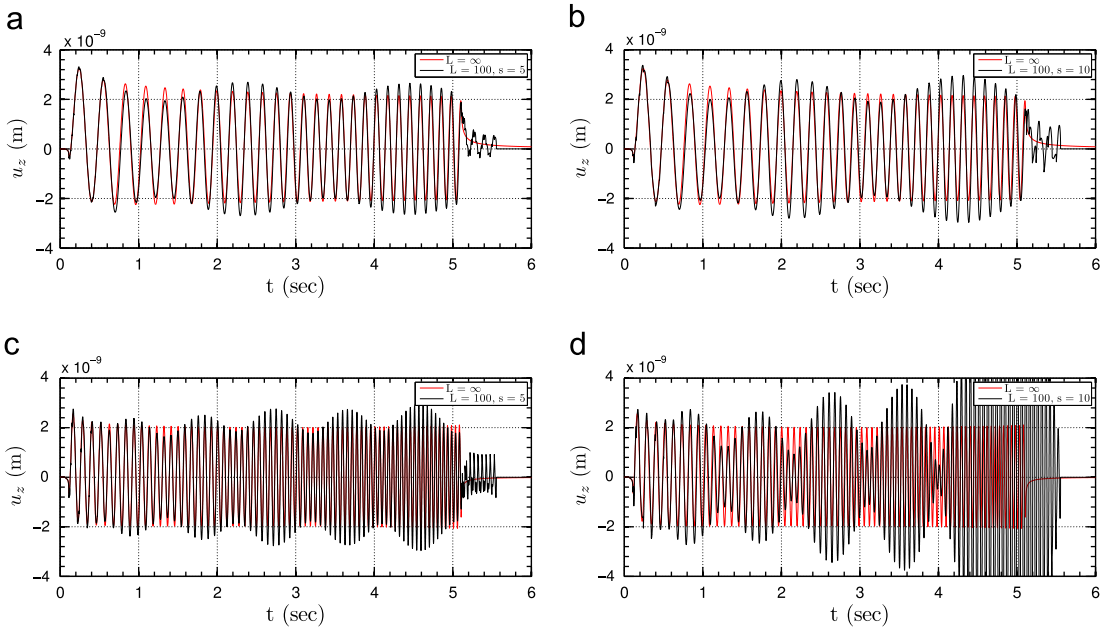

Fig. 16. Comparison of infinite line load ($L=\infty$), a continuous line load of finite length ($L=100$ m), and a series of point loads spaced s meters apart over a distance of 100 m: (a) $s=5$, chirp C-3-8; (b) $s=10$, chirp C-3-8; (c) $s=5$, chirp C-8-20; and (d) $s=10$, chirp C-8-20.

5.4.1. Representation of the line load by a few point loads

We replace next the continuous line load with equivalent, equidistant point sources, spaced s apart. In particular, we consider two values for s, 5 m, and 10 m, respectively, and run numerical experiments with the chirp signals of Table 2. The results for the first two chirps of Table 2 are shown in Fig. 16 and demonstrate good agreement between the case of a line load of infinite length and that of point sources, positioned 5 m apart from each other. The agreement is better for lower frequencies and deteriorates for higher frequencies. Hence, we choose $L=100$ m with $s=5$ m for the first two chirp signals of Table 2 in our field experiment (the 10 m spacing would lead to inaccuracies).

5.5. The experiment layout

We discuss next the actual field experiment aimed at a local characterization of the Hornsby Bend site located in Austin, TX,

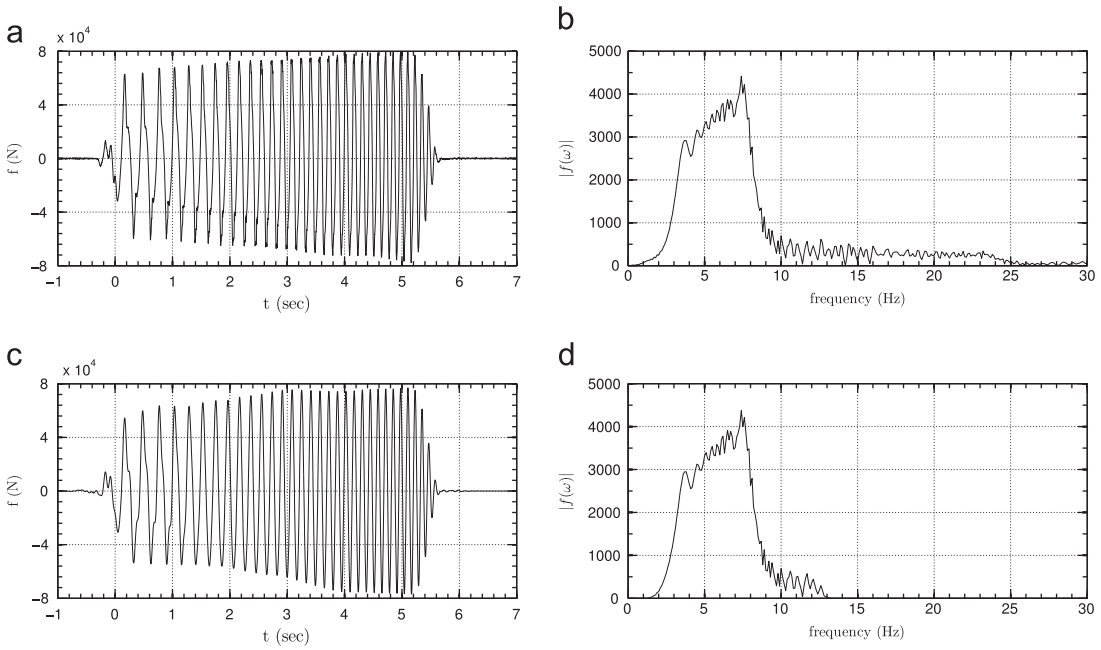

Fig. 18. Force (chirp C-3-8) applied by Liquidator at $(\xi_1,\xi_2)=(0,0)$: (a) time-history (recorded), (b) Fourier spectrum (recorded), (c) time-history (filtered) and (d) Fourier spectrum (filtered).

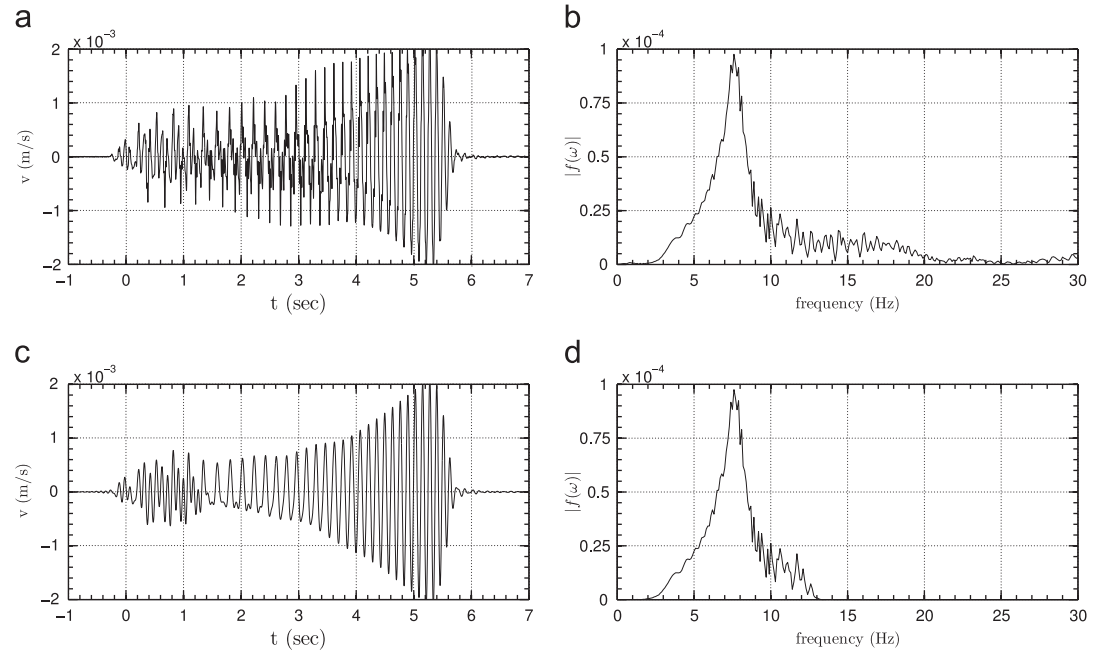

Fig. 19. Velocity (due to force C-3-8 at (0,0,0)) measured at $(-5,0,0)$: (a) time-history (recorded), (b) Fourier spectrum (recorded), (c) time-history (filtered) and (d) Fourier spectrum (filtered).

using the field data, and the inversion methodology code discussed. As discussed already, a key assumption is that the site enjoys symmetry along the sensor plane, as displayed in Fig. 8. Our objective is to explore a site of length 200 m along this plane. We place sensors every 5 m. These are shown in Fig. 17 with bullets. We consider sources, also spaced 5 m apart from each other, indicated by squares, which are placed along five lines of length 100 m. Due to the symmetry assumptions, we consider sources only on one side of the sensor plane, and assume that if we had sources on the mirror side, they would have yielded the same response as their existing counterparts. The experiment was performed in Austin, TX, Hornsby Bend in October 2010.

6. Field experiment records and data processing

In this section, we discuss a subset of the field recorded data, and outline the data processing procedure. The latter consists of two main parts. First, identification and reduction of noise effects associated with the recorded data, and second, integrating the

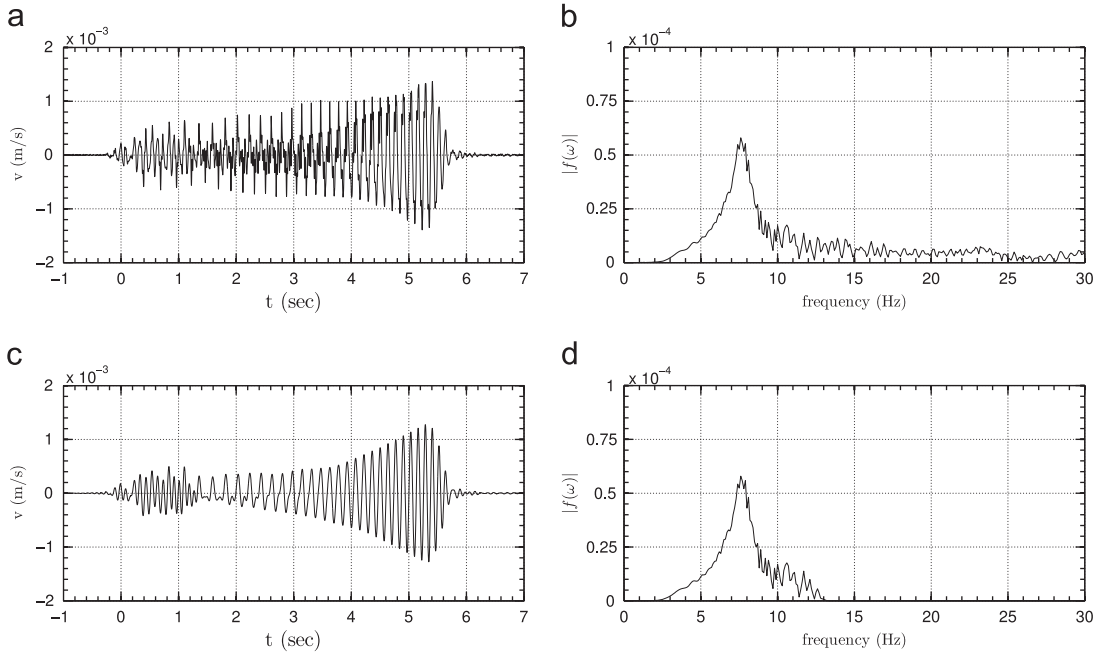

Fig. 20. Velocity (due to force C-3-8 at (0,−5,0)) measured at (−5,0,0): (a) time-history (recorded), (b) Fourier spectrum (recorded), (c) time-history (filtered) and (d) Fourier spectrum (filtered).

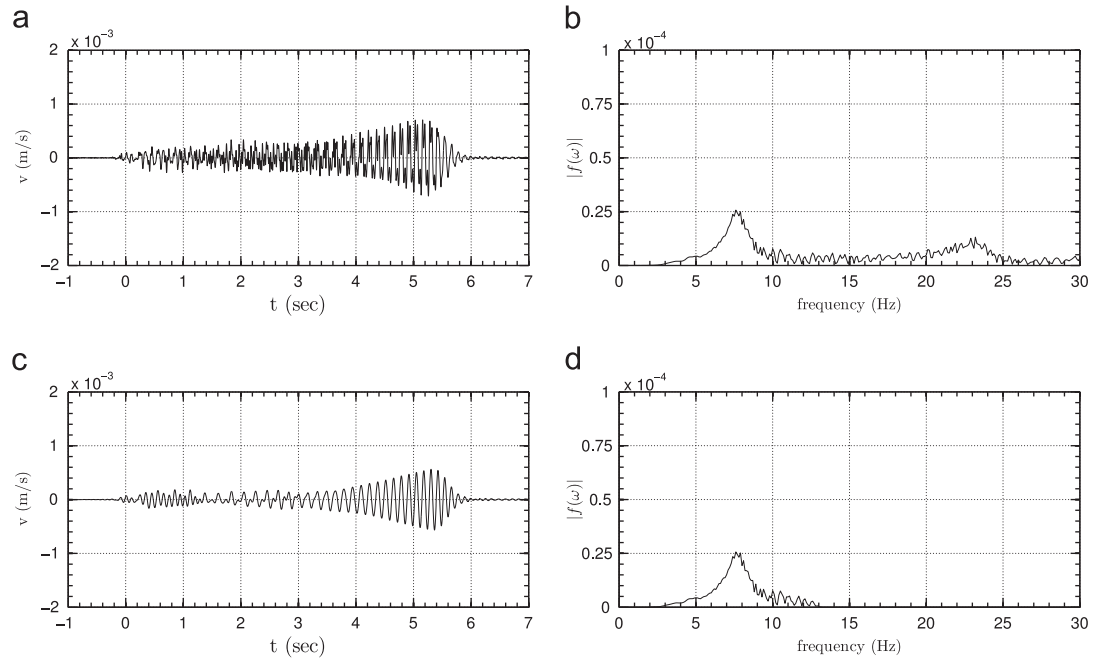

Fig. 21. Velocity (due to force C-3-8 at (0,−10,0)) measured at (−5,0,0): (a) time-history (recorded), (b) Fourier spectrum (recorded), (c) time-history (filtered) and (d) Fourier spectrum (filtered).

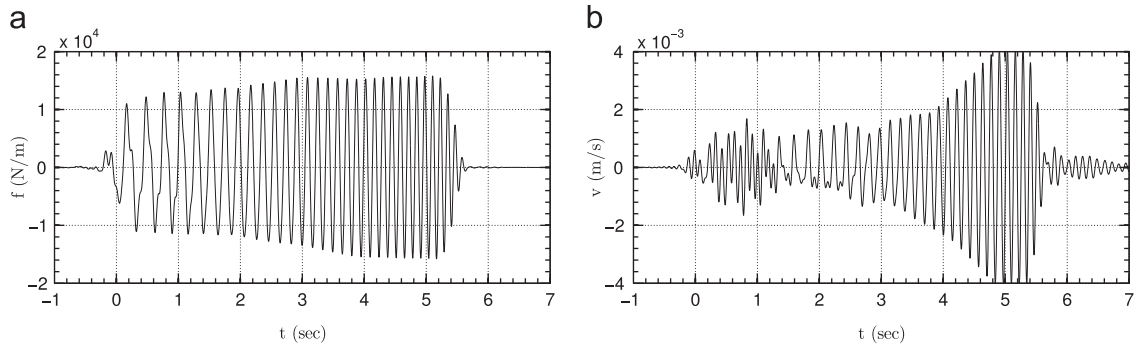

Fig. 22. Equivalent line load (chirp C-3-8) applied at $\xi_1 = 0$ m, and corresponding response at $x_1 = -5$ m: (a) force time-history and (b) velocity time-history.

data in such a way that they readily fit the requirements of our two-dimensional inversion codes.

6.1. Signal processing

Our records are inevitably contaminated by noise, which may distort the signals both at high and low frequencies. Our aim is to identify the parts of a signal (in the frequency domain), where the signal-to-noise ratio is low, and filter out these parts from the records. This is particularly important when dealing with low frequency noise, since the noise gets amplified when the velocity record is integrated to yield displacement time-history. The latter may look unphysical and necessitate baseline adjustment [1], which will have serious consequences in the inversion process. On the other hand, high frequency noise may be less of a concern due to the regularization terms in the inversion algorithm: the regularization terms make the objective functional less sensitive to the high frequency noise [21].

A sampling frequency of 820 Hz is used for digital data collection. Assuming the highly unlikely event that data being contaminated by noise up to a range of 100 Hz (noise was observed up to 70 Hz), a sampling rate of 200 Hz could prevent aliasing effects according to the Nyquist sampling theorem [16]. In this sense, we oversampled the data, which causes no harm. Moreover, in order to reduce the effects of ambient noise, we repeated each loading five times, and use the average in our analysis.

We favor finite impulse response (FIR) filters since they preserve a signal's phase information (linear phase), and do not result in phase distortion, as commonly occurs in more popular infinite impulse response (IIR) filters [16]. We use Matlab's equiripple bandpass filter, with high and low cuts of 2.5 Hz and 12 Hz, respectively, and high and low slopes of 60 dB/octave and 38 db/octave, for the C-3-8 chirp (see Table 2). For the C-8-20 chirp, we use the same type of filter, with high and low cuts of 2.5 Hz and 25 Hz, and high and low slopes of 60 dB/octave and 26 db/octave, respectively.

Next, we present some of the field experiment records both in their unprocessed and processed form. For example, Fig. 18 shows the C-3-8 chirp, applied by Liquidator at $(\xi_1,\xi_2) = (0,0)$. The record may be compared with the record in Fig. 14, which is the corresponding theoretical curve. Notice that the applied load lies mainly within the design frequency range, except for the relatively small-component high-frequency noise, which probably originates with the Liquidator's engine and hydraulics. Figs. 19–21 depict a subset of the recorded sensor data: both unprocessed and processed (filtered) velocity records are shown for various sensor locations due to different loads. In all cases shown, the load is the chirp C-3-8, as shown earlier in Fig. 18. Shown in Figs. 19–21 are the velocity time-histories at $(-5,0,0)$, while the load is applied at $(0,0,0)$, $(0,-5,0)$, and $(0,-10,0)$, respectively. Geometric decay is noticeable and amplitude reduction in velocity time-history is observed as distance between the source and observer increases.

6.2. Data integration

In this section, we address how we use the, essentially, three-dimensional field data, in order to obtain records suitable for exercising our two-dimensional codes. We follow the same lines as in the experiment design. Similar to what we did in (42), we obtain the following equivalent two-dimensional velocity time history v^{2L} from the three-dimensional field-recorded $v^{3D} := v^{3D}(x_1,x_2,t;\xi_1,\xi_2)$:

$$v^{2L}(x_1,t;\xi_1,\xi_2) = v^{3D}(x_1,0,t;\xi_1,0) + 2\sum_{j=1}^{m} v^{3D}(x_1,0,t;\xi_1,js), \tag{43}$$

where x_1 denotes a geophone's location along the x_1-axis, (ξ_1,ξ_2) denotes the load location, $m(=20)$ is the number of source locations for which $x_2 > 0$, and $s = 5$ m is the distance between the loads. v^{2L} is the equivalent two-dimensional velocity record, which can then be integrated in time to yield the displacement time history. Similarly, for the equivalent two-dimensional force time history, we obtain

$$f^{2L}(\xi_1,t) = \frac{1}{(2m+1)s}\left[f^{3D}(\xi_1,0,t) + 2\sum_{j=1}^{m} f^{3D}(\xi_1,js,t)\right], \tag{44}$$

where $f^{3D}(\xi_1,\xi_2,t)$ denotes the measured force applied at any given location (ξ_1,ξ_2). For example, the equivalent line load corresponding to chirp C-3-8, applied at $\xi_1 = 0$, and the resulting velocity time history at $x_1 = -5$ m are depicted in Fig. 22. The data, both measured force and recorded response, with the aid of (43) and (44), can now be readily used for inversion.

7. Inversion results using field experiment data

In this section, we use the inversion theory discussed earlier, along with the measured data from the field experiment, to arrive at an estimate of the spatial distribution of the P- and S-wave velocities at the target site (Hornsby Bend).

The target domain is a two-dimensional slice, 200 m wide and 48 m deep. The domain is surrounded on its sides and bottom by a 10 m-thick PML to absorb outgoing waves. We use bilinear quadrilateral elements with element size of 1 m when applying the C-3-8 chirp (see Table 2), whereas 8-noded serendipity elements of the same size are used for higher frequency chirps. In all cases, we use 1 m × 1 m bilinear quadrilateral elements to interpolate the material properties.

According to the experiment layout in Fig. 17, we apply loads at every 5 m along five lines. T-Rex was used for loading along the lines $x_1 = -60$ m, $+30$ m, and $+60$ m, whereas Liquidator was used to load along $x_1 = -30$ m, and 0 m. We used 36 geophones with a resonant frequency of 1 Hz at every 5 m, along the x_1-axis. After processing the recorded data, per the discussion of the preceding section, we proceeded with the inversion process.

7.1. Inversion process

The inversion process begins with an initial profile for both of the Lamé parameters (linear in depth or homogeneous), and iteratively updates the profile until the misfit between the measured response and the computed response obtained at each inversion iteration is minimized. The convergence rate of the inversion process to the target profile, and even the success of the process itself, depends greatly on the initial guess, as is typically the case. An initial profile, which is close to the target profile, will likely need a fewer number of iterations to converge, compared to an arbitrary initial profile. This fact can be exploited to speed up the convergence. If, for example, during a field experiment, an SASW experiment is performed in addition to the data collection for the full waveform inversion approach, then the SASW-rendered profile could be used as initial guess for the full waveform inversion. The SASW profile will be, by definition, horizontally layered, whereas the full waveform-based inverted profile will be, in general, arbitrarily heterogeneous.

We start the inversion process by applying the first (measured) equivalent force corresponding to chirp C-3-8 (see Table 2 for the theoretical curve and Fig. 22 for the actual, equivalent measured force). There are 5 loads at our disposal, and 36 measuring locations for every load. Owing to linearity, we apply all 5 loads simultaneously and add their corresponding responses at every sensor location. Other possibilities for combining the loads also exist [6,18].

Due to the very construction of the chirp signals, their frequency increases linearly with time. This may be exploited to further regularize the inversion process, i.e., we start the inversion process by considering only a portion of the total chirp duration, arrive at an inverted profile, use the inverted profile as an initial guess to the next round of inversion, where we increase the duration of the same chirp signal, thus, gradually, bringing additional frequencies to bear

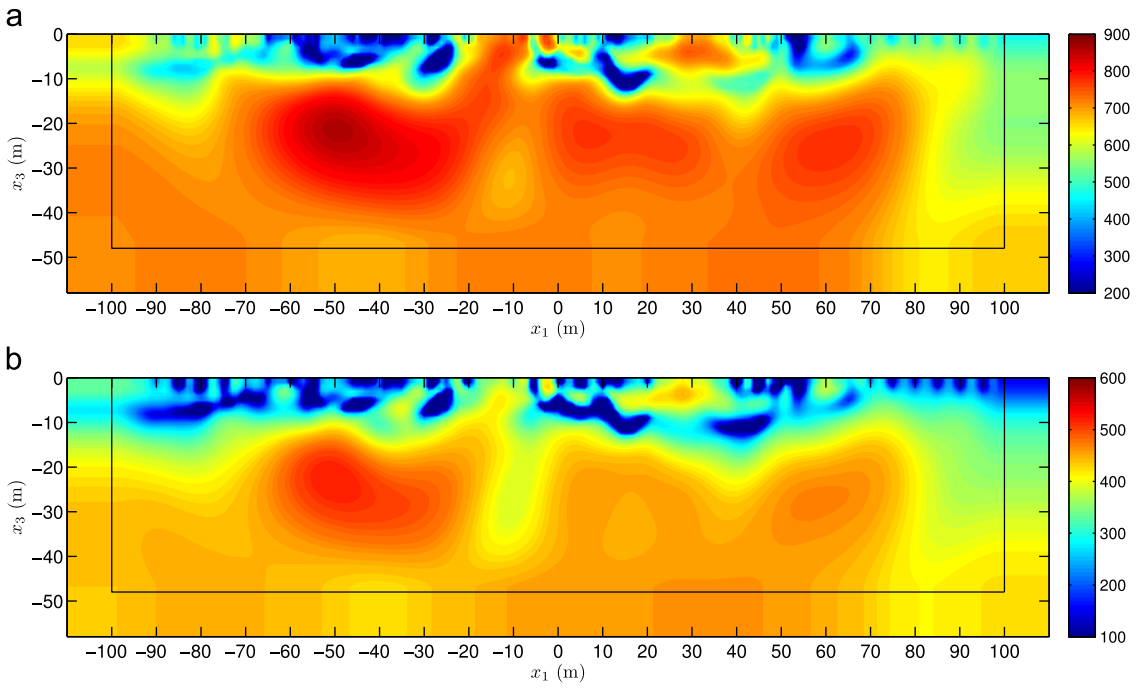

Fig. 23. Inverted profiles for c_p and c_s at iteration 1900: (a) $c_p(m/s)$ and (b) $c_s(m/s)$.

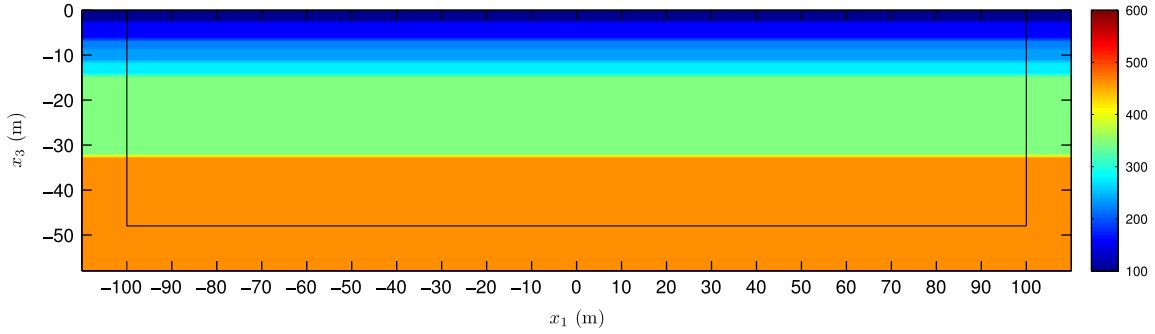

Fig. 24. Inverted profile for c_s via the SASW method.

on the inversion process (a, so-called, continuation scheme). For example, for the site under study, we start with the first 2 s of the signals, and progressively move up to 7 s duration, in increments of 1 s. A similar idea was discussed in [11,12].

After 1900 iterations, the misfit between the measured response and the computed response becomes small enough, with no discernible update in the material properties. The corresponding compressional and shear wave velocity profiles for the Hornsby

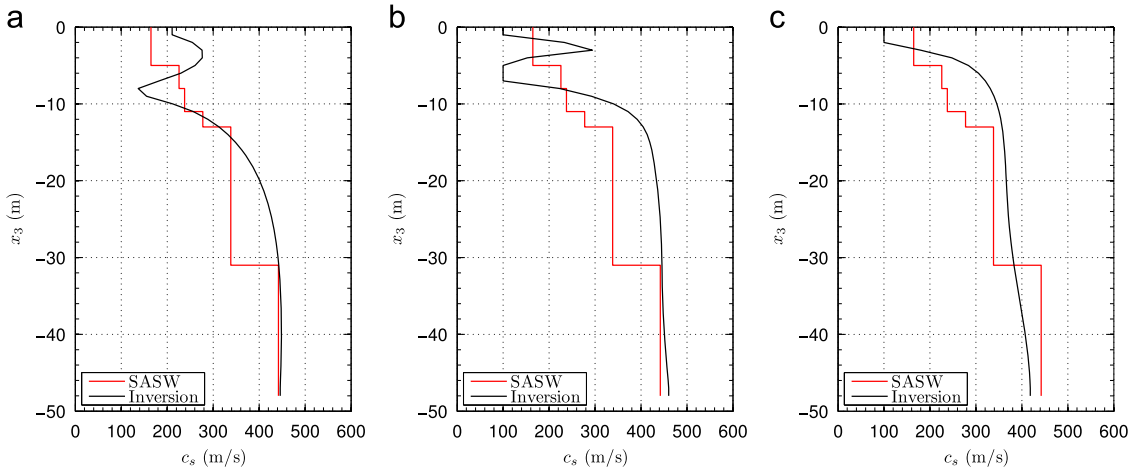

Fig. 25. Shear wave velocity profiles obtained via SASW and full waveform-based inversion: (a) $x_1 = -90$ m, (b) $x_1 = \pm 0$ m and (c) $x_1 = +90$ m.

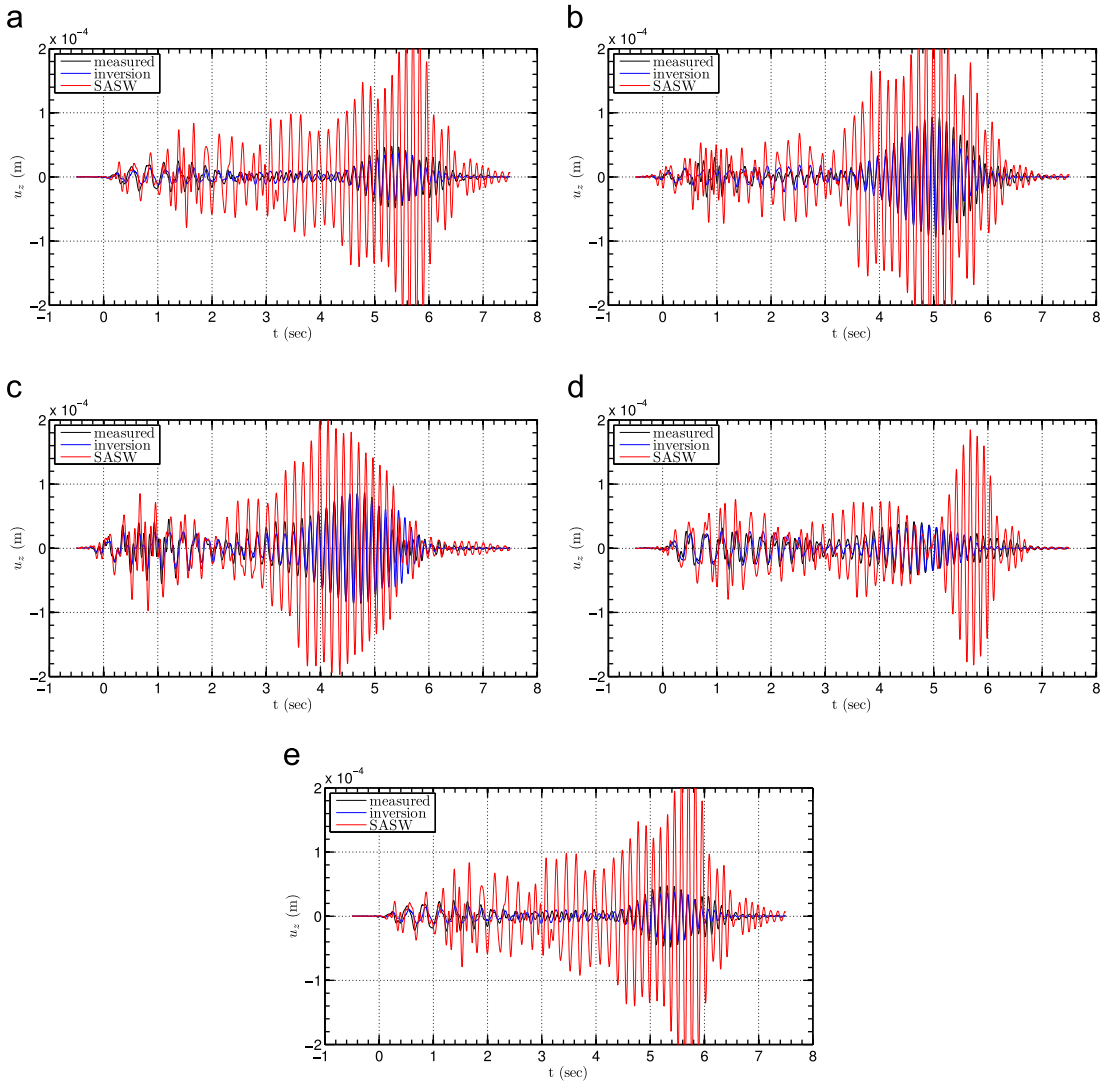

Fig. 26. Comparison of measured surface displacement time-histories against those resulting from the SASW and full waveform-based inversion: (a) $x_1 = -80$ m, (b) $x_1 = -40$ m, (c) $x_1 = +5$ m, (d) $x_1 = +35$ m and (e) $x_1 = +70$ m.

Bend site are shown in Fig. 23 (a constant mass density of $\rho = 2000\ \mathrm{kg/m^3}$ is considered for the soil medium throughout the analysis).

7.2. Comparison with SASW

Next, we compare our shear wave velocity (c_s) profile with that obtained via the SASW method. The Spectral-Analysis-of-Surface-Waves method relies on the dispersive nature of Rayleigh wave velocity in layered media, i.e., the propagation speed of the surface waves depends on the frequency of the load [19]. Measuring this wave speed for different frequencies in a field experiment results in the experimental dispersion curve. Next, a theoretical dispersion curve can be computed for a homogeneous elastic layered medium. The material properties for each layer are varied until a match is attained between the experimental and the theoretical dispersion curve (a comprehensive description of the SASW method can be found in [3]). The method assumes that the dominant portion of the wave energy is transported through Rayleigh waves, and disregards other wave types such as compressional and shear waves. The SASW is capable of rendering only horizontally layered profiles and only of the shear wave velocity. Despite its limitations it is widely used.

We performed three SASW experiments at our site: at the centerpoint $(x_1,x_2) = (0,0)$ and close to the two end points of the domain $(x_1,x_2) = (\pm 90,0)$. The c_s profile corresponding to the center point is shown in Fig. 24, whereas Fig. 25 compares the SASW profile with those obtained from the inversion process at the $x_1 = -90$ m, 0 m, and $+90$ m cross-sectional lines of the domain. In general, there is good agreement between the two methods. Discrepancies may be attributed to the three-dimensional nature of the physical problem. While in our study, we use a two-dimensional model for the full waveform inversion, the model is one-dimensional for the SASW method. Whereas there may exist lateral property variability in the actual physical problem, these effects are completely neglected in the SASW method, and are only partially accounted for in the two-dimensional inversion process. We also observe that while the SASW method predicts sharp profile changes in depth, the inversion process yields profiles that vary gradually. Indeed, this is due to the Tikhonov regularization scheme, which precludes high gradients in the material profile while allowing smooth spatial variations.

We also compute time-history results corresponding to numerical simulation of the medium based on profiles obtained from the inversion process and the SASW method, and compare them with the actual field measurements at a few locations. To this end, since the SASW method only yields the shear wave velocity of the soil medium, we supplemented it with an estimation of the compressional wave velocity, by assuming that the Poisson ratio decreases from 0.35 on the ground surface to 0.25 at a depth of -50 m. This allowed us to compute the response at the ground surface using the SASW-rendered profile. Due to the small variability between the

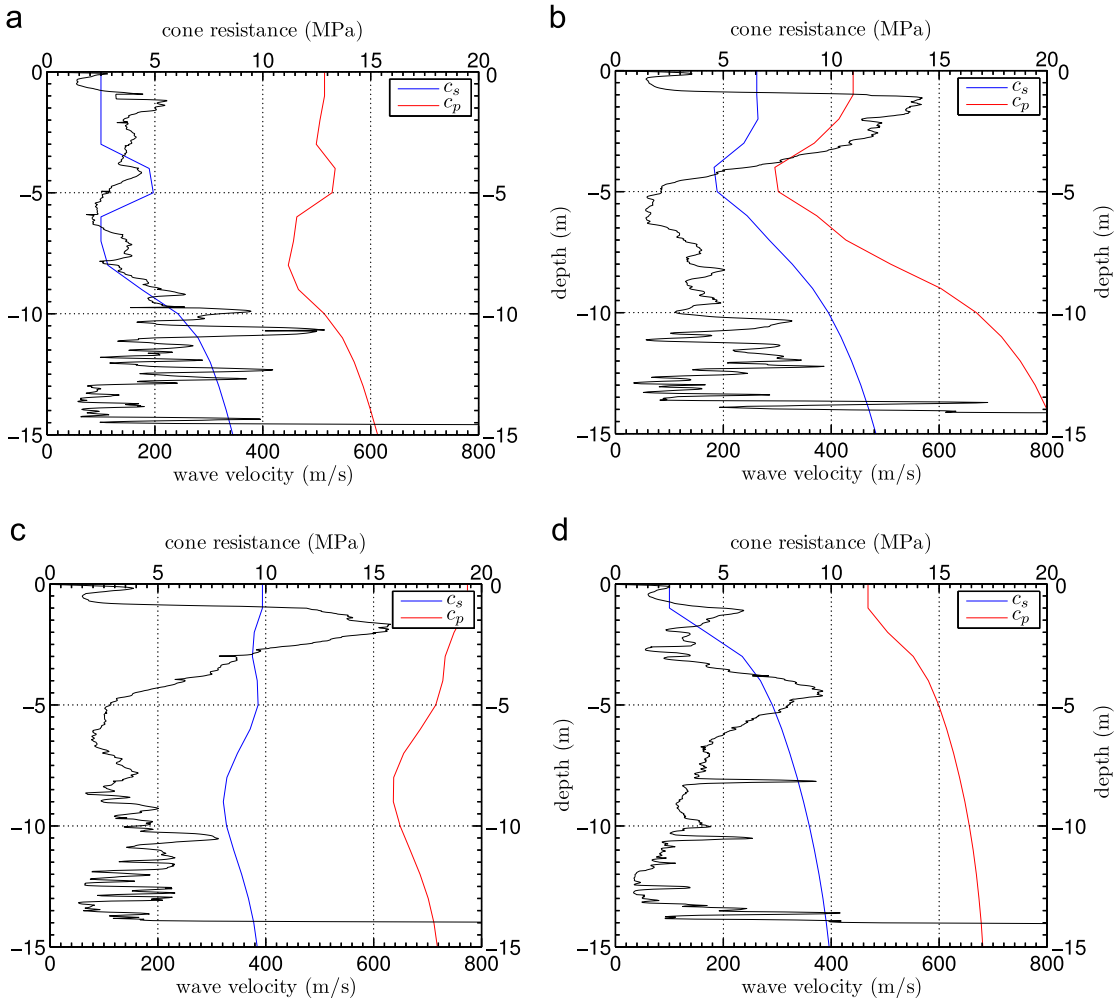

Fig. 27. Juxtaposition of CPT results and the inverted profiles: (a) $x_1 = -80$ m, (b) $x_1 = -50$ m, (c) $x_1 = -8$ m and (d) $x_1 = +80$ m.

three SASW profiles, we use their average in the time-history analysis for simplicity. Displacement time-histories at $x_1 = -80$ m, -40 m, 5 m, $+35$ m, and $+70$ m are shown in Fig. 26. Excellent agreement can be observed between the time histories computed based on the full waveform inverted profile and the true recorded motion, whereas the SASW-based time histories exhibit significant amplitude discrepancies. We should mention, however, that since the full waveform inversion process forces time-history matching, this may not be a fair comparison.

7.3. Comparison with cone penetration test (CPT) results

The cone penetration test (CPT) is an intrusive field experiment which provides information on soil properties and the soil's stratification. A rod with a cone-shaped ending is forced into the ground at a constant rate, while two load cells measure the required load that drives the rod into the ground. The first load cell measures the force that acts directly on the cone and yields the cone resistance, which is obtained by dividing the force over the cone's area. The second load cell measures the force that acts on the lateral sides of the rod, immediately past the cone, and provides sleeve friction [10]. Unfortunately, CPT results cannot be correlated with elastic properties of the soil. However, the cone resistance is an indicator of soil stiffness, and the depth at which the cone cannot be forced further into the ground, corresponds to a stiff layer. We present CPT results at the same site, and consider mainly the qualitative information that the test provides.

We performed CPT tests at four sample locations to investigate if they hit the stiff zones predicted by the inverted profile. These locations are at the $x_1 = -80$ m, -50 m, -8 m, and $+80$ m cross-sectional lines of the domain. The cone resistance along depth at these locations is shown in Fig. 27, along with the inverted c_p and c_s profiles. It can be observed that the cone cannot be pushed any further once it reaches a zone where the shear wave velocity is approximately around 400 m/s. There is general agreement between the CPT results and the inverted profile. For instance, at $x_1 = -80$ m, the cone resistance and the shear wave velocity have the same pattern in depth. At $x_1 = -50$ m, cone resistance has a spike at a shallow depth, reaches its minimum value at a depth of 5 m, and increases again after that. We observe a similar trend for both the shear and the compressional wave velocities. It is difficult to find a correlation at $x_1 = -8$ m and $+80$ m.

8. Conclusions

We discussed recent advances in the development of a general and robust methodology for geotechnical site characterization based on full waveform inversion. We complemented the theory and the numerical implementation with numerical results derived not only from synthetic data but also from field data. To the best of our knowledge, this is the first attempt that field data have been successfully used for geotechnical site characterization using full waveform inversion techniques.

A focal point of this communication dealt with the design and post-processing needs of the field experiment, so that collected records can be seamlessly integrated into the software toolchain. In this paper, we dealt exclusively with two-dimensional site characterization. We assumed that the site under investigation can be idealized as a plane strain problem, which clearly poses a restriction on the applicability of our software. However, extension to three dimensions is straightforward and will be addressed in future communications.

Our results are in good agreement with the widely used SASW method, with the clear advantage of allowing for arbitrary profile heterogeneity, as opposed to the one-dimensional character of the SASW technique. We have also demonstrated how this technology can be used in practice by discussing various elements involved in an industrial-scale field experiment.

Key elements of this development include:

- Efficient numerical simulations of forward wave motion within the arbitrarily heterogeneous near-surface deposits that accurately capture the underlying physics. To this end, the site under study is truncated using state-of-the-art perfectly-matched-layers, and a hybrid finite element technique is used to resolve the motion within the interior domain and the PML buffer (standard Galerkin for the interior domain coupled with a non-classically mixed for the PML).
- Tackling of the inverse medium problem via a PDE-based optimization apparatus, where we favor a discretize-then-optimize implementation of the associated adjoint and control problems due to its numerical robustness. Moreover, we tackle ill-posedness and solution multiplicity through an appropriate regularization approach (Tikhonov) and via a continuation scheme that allows the gradual probing of the domain with signals of the increasing frequency content.
- Development of a simple procedure for the design of a field experiment that is well coupled with the algorithmic development.

Overall, our full waveform inversion-based site characterization methodology seems robust and promising. The framework we discussed is systematic, and can be applied to the more realistic three-dimensional case without major modifications; the key challenge is in the computational efficiency.

Acknowledgments

It is with great pleasure that the writers contribute this paper to the special issue of Soil Dynamics and Earthquake Engineering honoring Professor José M. Roësset. We respectfully acknowledge the important contributions Professor Roësset has made throughout his career to the understanding of soil–structure interaction and to the development of associated modeling technologies, which have influenced generations of engineers. Our own ages span several decades: whether young or seasoned, we too have benefited from Professor Roësset's writings, his ideas, his advice, and his great sense of humor.

The second author also wishes to acknowledge the many helpful discussions on inversion he had with Dr. Georg Stadler of the Institute for Computational Engineering and Sciences at the University of Texas at Austin. We also wish to thank Dr. Y.-C. Lin and Mr. Changyoung Kim of the University of Texas at Austin for assisting with the processing of the SASW field test results, and the CPT tests, respectively. Support for the authors' research has been provided by the National Science Foundation under a NEESR-SG grant award (CMMI-0619078). This support is gratefully acknowledged.

Appendix A

A.1. On the third discrete optimality condition

We discuss the derivation of the discrete control equations, i.e., of the third discrete optimality condition, given in (29) and (30). We take the derivative of $\mathcal{L}$ with respect to $\boldsymbol{\lambda}$ and $\boldsymbol{\mu}$ over the interior domain only, since the values of the Lamé parameters at the interface nodes are extended into the PML domain, without any variation along the direction of projection [7]. This assumption greatly simplifies the derivation and implementation of the control equations.

A.1.1. The λ control problem

Eq. (1) governs the interior domain, denoted by Ω^{RD}, where λ,μ contribute only to terms in the $\boldsymbol{K}$ matrix of (9), which contributes to $\boldsymbol{Q}$ in (13). We denote the part of $\boldsymbol{K}$ that belongs to the interior domain by $\boldsymbol{K}^{\mathrm{RD}}$: it is the stiffness matrix of the interior problem, and is given by [9]:

$$\boldsymbol{K}^{\mathrm{RD}}=\int_{\Omega^{\mathrm{RD}}}\begin{bmatrix}(\boldsymbol{\lambda}^T\boldsymbol{\chi}+2\boldsymbol{\mu}^T\boldsymbol{\chi})\boldsymbol{\Phi}_{x_1}\boldsymbol{\Phi}_{x_1}^T+(\boldsymbol{\mu}^T\boldsymbol{\chi})\boldsymbol{\Phi}_{x_3}\boldsymbol{\Phi}_{x_3}^T & \dots & (\boldsymbol{\lambda}^T\boldsymbol{\chi})\boldsymbol{\Phi}_{x_1}\boldsymbol{\Phi}_{x_3}^T+(\boldsymbol{\mu}^T\boldsymbol{\chi})\boldsymbol{\Phi}_{x_3}\boldsymbol{\Phi}_{x_1}^T\\ (\boldsymbol{\lambda}^T\boldsymbol{\chi})\boldsymbol{\Phi}_{x_3}\boldsymbol{\Phi}_{x_1}^T+(\boldsymbol{\mu}^T\boldsymbol{\chi})\boldsymbol{\Phi}_{x_1}\boldsymbol{\Phi}_{x_3}^T & \dots & (\boldsymbol{\lambda}^T\boldsymbol{\chi}+2\boldsymbol{\mu}^T\boldsymbol{\chi})\boldsymbol{\Phi}_{x_3}\boldsymbol{\Phi}_{x_3}^T+(\boldsymbol{\mu}^T\boldsymbol{\chi})\boldsymbol{\Phi}_{x_1}\boldsymbol{\Phi}_{x_1}^T\end{bmatrix}d\Omega^{\mathrm{RD}},\tag{45}$$

where $\boldsymbol{\chi}$ is the vector of interpolation functions for the Lamé parameters, $\boldsymbol{\Phi}$ are the displacement interpolants, and subscripts x_1,x_3 denote differentiation with respect to x_1, and x_3, respectively. Taking the derivative of $\boldsymbol{K}^{\mathrm{RD}}$ with respect to $\boldsymbol{\lambda}$ yields

$$\frac{\partial\boldsymbol{K}^{\mathrm{RD}}}{\partial\boldsymbol{\lambda}}=\int_{\Omega^{\mathrm{RD}}}\begin{bmatrix}\boldsymbol{\Phi}_{x_1}\boldsymbol{\Phi}_{x_1}^T\boldsymbol{\chi} & \boldsymbol{\Phi}_{x_1}\boldsymbol{\Phi}_{x_3}^T\boldsymbol{\chi}\\ \boldsymbol{\Phi}_{x_3}\boldsymbol{\Phi}_{x_1}^T\boldsymbol{\chi} & \boldsymbol{\Phi}_{x_3}\boldsymbol{\Phi}_{x_3}^T\boldsymbol{\chi}\end{bmatrix}d\Omega^{\mathrm{RD}},\tag{46}$$

which are the building blocks of $\partial\boldsymbol{Q}/\partial\boldsymbol{\lambda}$ in (29), thus enabling its computation.

A.1.2. The μ control problem

In a way similar to what we did above, we take the derivative of $\boldsymbol{K}^{\mathrm{RD}}$ with respect to $\boldsymbol{\mu}$ to obtain

$$\frac{\partial\boldsymbol{K}^{\mathrm{RD}}}{\partial\boldsymbol{\mu}}=\int_{\Omega^{\mathrm{RD}}}\begin{bmatrix}[2\boldsymbol{\Phi}_{x_1}\boldsymbol{\Phi}_{x_1}^T+\boldsymbol{\Phi}_{x_3}\boldsymbol{\Phi}_{x_3}^T]\boldsymbol{\chi} & \boldsymbol{\Phi}_{x_3}\boldsymbol{\Phi}_{x_1}^T\boldsymbol{\chi}\\ \boldsymbol{\Phi}_{x_1}\boldsymbol{\Phi}_{x_3}^T\boldsymbol{\chi} & [2\boldsymbol{\Phi}_{x_3}\boldsymbol{\Phi}_{x_3}^T+\boldsymbol{\Phi}_{x_1}\boldsymbol{\Phi}_{x_1}^T]\boldsymbol{\chi}\end{bmatrix}d\Omega^{\mathrm{RD}},\tag{47}$$

thus allowing the computation of $\partial\boldsymbol{Q}/\partial\boldsymbol{\mu}$ in (30).

A.2. On the spatial integration of (40)

We assume that the line load is applied along the x_2-axis with a total length of $2L$, and that the observer is positioned along the x_1-axis. We make the following change of variable to ease the analytical integration:

$$G^{2L}(x_1,t)=\int_{-L}^{L}G^{3D}(x_1,x_2,t)\,dx_2=2\int_{x_1}^{r_L}G^{3D}(r,t)\frac{r}{\sqrt{r^2-x_1^2}}\,dr,\tag{48}$$

where $r=\sqrt{x_1^2+x_2^2}$, $r_L=\sqrt{x_1^2+L^2}$, and Green's function G^{3D} is given as

$$G^{3D}(r,t)=B(r)\begin{cases}0, & \tau<a,\\ u_1, & a\le\tau\le 1,\\ u_2^*, & 1\le\tau\le\xi_3,\\ 1, & \tau>\xi_3,\end{cases}\tag{49}$$

We have the following definitions:

$$B(r)=\frac{1}{r}B^*=\frac{1}{r}\frac{1-\nu}{2\pi\mu},\quad \tau=t\frac{c_s}{r},$$

$$u_1=\frac{1}{2}-\frac{1}{2}\sum_{i=3}^{3}\frac{A_i}{\sqrt{|\tau^2-\xi_i^2|}},\quad u_2^*=1-\frac{A_3}{\sqrt{\xi_3^2-\tau^2}},$$

$$a=\sqrt{\frac{1-2\nu}{2-2\nu}},\quad A_i=\frac{(1-2\xi_i^2)^2\sqrt{|a^2-\xi_i^2|}}{4(\xi_i^2-\xi_j^2)(\xi_i^2-\xi_k^2)},$$

where ν is Poisson's ration, μ is the shear modulus, c_s is the shear wave velocity, and ξ_i are the roots of the Rayleigh function:

$$R(\xi^2)=(2\xi^2-1)^2+4\sqrt{\xi^2-a^2}\sqrt{\xi^2-1}=0.$$

The above relations are valid when $\nu<0.2631$. In such a case, all roots are real and satisfy $0<\xi_1^2<\xi_2^2<a^2<1<\xi_3^2$ [5]. Making use of Heaviside functions, we rewrite (49) as follows:

$$G^{3D}(r,t)=B(r)\left\{-u_1H\left(r-\frac{tc_s}{a}\right)+(u_1-u_2^*)H\left(r-\frac{tc_s}{1}\right)+(u_2^*-1)H\left(r-\frac{tc_s}{\xi_3}\right)+1\right\}.\tag{50}$$

Substituting (50) into (48) yields

$$G^{2L}(x_1,t)=2(I_1+I_2+I_3+I_4),\tag{51}$$

where

$$I_1=\frac{1}{2}B^*\left\{\int_{x_1}^{r_L}\frac{-H\left(r-\frac{tc_s}{a}\right)}{\sqrt{r^2-x_1^2}}+\sum_{i=1}^{3}\int_{x_1}^{r_L}\frac{A_irH\left(r-\frac{tc_s}{a}\right)}{\xi_i\sqrt{\left(\frac{t^2c_s^2}{\xi_i^2}-r^2\right)(r^2-x_1^2)}}\,dr\right\},$$

$$I_2=\frac{1}{2}B^*\left\{\int_{x_1}^{r_L}\frac{-H\left(r-\frac{tc_s}{1}\right)}{\sqrt{r^2-x_1^2}}-\sum_{i=1}^{2}\int_{x_1}^{r_L}\frac{A_irH\left(r-\frac{tc_s}{1}\right)}{\xi_i\sqrt{\left(\frac{t^2c_s^2}{\xi_i^2}-r^2\right)(r^2-x_1^2)}}\,dr+\int_{x_1}^{r_L}\frac{A_3rH\left(r-\frac{tc_s}{1}\right)}{\xi_3\sqrt{\left(\frac{t^2c_s^2}{\xi_3^2}-r^2\right)(r^2-x_1^2)}}\,dr\right\},$$

$$I_3=B^*\int_{x_1}^{r_L}\frac{-A_3rH\left(r-\frac{tc_s}{\xi_3}\right)}{\xi_3\sqrt{\left(\frac{t^2c_s^2}{\xi_3^2}-r^2\right)(r^2-x_1^2)}}\,dr,$$

$$I_4=B^*\int_{x_1}^{r_L}\frac{dr}{\sqrt{r^2-x_1^2}}.$$

It is easy to verify that I_1, I_2, I_3, and I_4 consist of the following integrals with the corresponding closed-form solution:

$$F_1=\int\frac{rH\left(r-\frac{tc_s}{\lambda}\right)}{\sqrt{\left(r^2-\frac{t^2c_s^2}{\xi^2}\right)(r^2-x_1^2)}}\,dr=\frac{1}{2}H\left(r-\frac{tc_s}{\lambda}\right)\times\ln\left\{\frac{(r^2-x_1^2)+\left(r^2-\frac{t^2c_s^2}{\xi^2}\right)+2\sqrt{\left(r^2-\frac{t^2c_s^2}{\xi^2}\right)(r^2-x_1^2)}}{\left(\frac{t^2c_s^2}{\lambda^2}-x_1^2\right)+\left(\frac{t^2c_s^2}{\lambda^2}-\frac{t^2c_s^2}{\xi^2}\right)+2\sqrt{\left(\frac{t^2c_s^2}{\lambda^2}-\frac{t^2c_s^2}{\xi^2}\right)\left(\frac{t^2c_s^2}{\lambda^2}-x_1^2\right)}}\right\},$$

$$F_2 = \int \frac{rH\left(r-\frac{tc_s}{\lambda}\right)}{\sqrt{-\left(r^2-\frac{t^2c_s^2}{\xi^2}\right)(r^2-x_1^2)}}\,dr$$

$$= -\frac{1}{2}H\left(r-\frac{tc_s}{\lambda}\right)\left[\tan^{-1}\left\{\frac{\left(\frac{t^2c_s^2}{\xi^2}-r^2\right)+(x_1^2-r^2)}{2\sqrt{\left(\frac{t^2c_s^2}{\xi^2}-r^2\right)(r^2-x_1^2)}}\right\}\right.$$

$$\left.-\tan^{-1}\left\{\frac{\left(\frac{t^2c_s^2}{\xi^2}-\frac{t^2c_s^2}{\lambda^2}\right)+\left(x_1^2-\frac{t^2c_s^2}{\lambda^2}\right)}{2\sqrt{\left(\frac{t^2c_s^2}{\xi^2}-\frac{t^2c_s^2}{\lambda^2}\right)\left(\frac{t^2c_s^2}{\lambda^2}-x_1^2\right)}}\right\}\right],$$

$$F_3 = \int \sqrt{r^2-x_1^2}\,dr = \ln(r+\sqrt{r^2-x_1^2}),$$

$$F_4 = \int H\left(r-\frac{tc_s}{\lambda}\right)\sqrt{r^2-x_1^2}\,dr = H\left(r-\frac{tc_s}{\lambda}\right)\left\{\frac{\ln(r+\sqrt{r^2-x_1^2})}{\ln\left(\frac{tc_s}{\lambda}+\sqrt{\frac{t^2c_s^2}{\lambda^2}-x_1^2}\right)}\right\},$$

where λ takes the value of a,1, or ξ_3. Clearly, by exploiting the above closed-form expressions, (40) can be evaluated accurately and efficiently.

References

[1] Boore DM, Bommer JJ. Processing of strong-motion accelerograms: needs, options and consequences. Soil Dynamics and Earthquake Engineering 2005;25:93–115.

[2] Gunzburger MD. Perspectives in flow control and optimization, advances in design and control. Philadelphia, PA: Society for Industrial and Applied Mathematics (SIAM); 2003.

[3] Joh SH. Advances in the data interpretation technique for spectral-analysis-of-surface-waves (SASW) measurements. PhD thesis, The University of Texas at Austin; 1996.

[4] Kang JW, Kallivokas LF. The inverse medium problem in heterogeneous PML-truncated domains using scalar probing waves. Computer Methods in Applied Mechanics and Engineering 2011;200:265–83.

[5] Kausel E. Fundamental solutions in elastodynamics: a compendium. New York, NY: Cambridge University Press; 2006.

[6] Krebs JR, Anderson JE, Hinkley D, Neelamani R, Lee S, Baumstein A, et al. Fast full-wavefield seismic inversion using encoded sources. Geophysics 2009;74: WCC177–88.

[7] Kucukcoban S. The inverse medium problem in PML-truncated elastic media. PhD thesis, The University of Texas at Austin, 2010.

[8] Kucukcoban S, Kallivokas LF. Mixed perfectly-matched-layers for direct transient analysis in 2d elastic heterogeneous media. Computer Methods in Applied Mechanics and Engineering 2011;200:57–76.

[9] Kucukcoban S, Kallivokas LF. A symmetric hybrid formulation for transient wave simulations in PML-truncated heterogeneous media. Wave Motion 2013;50:57–79.

[10] Lunne T, Robertson PK, Powell JJM. Cone penetration testing in geotechnical practice. London: Spon Press; 2002.

[11] Meles G, Greenhalgh S, van der Kruk J, Green A, Mauerer H. Taming the non-linearity problem in GPR full-waveform inversion for high contrast media. Journal of Applied Geophysics 2012;78:31–43.

[12] Na S-W, Kallivokas LF. Direct time-domain soil profile reconstruction for one-dimensional semi-infinite domains. Soil Dynamics and Earthquake Engineering 2009;29:1016–26.

[13] Nocedal J, Wright S. Numerical optimization. Springer series in operations research. 2nd ed. Springer, New York, NY, 2006.

[14] Park CB, Miller RD, Xia J. Multichannel analysis of surface waves. Geophysics 1999;64:800–8.

[15] Petra N, Stadler G. Model variational inverse problems governed by partial differential equations. ICES Report 11-05. The Institute for Computational Engineering and Sciences, The University of Texas at Austin, 2011.

[16] Proakis JG, Manolakis DK. Digital signal processing. 4th ed. Englewood Cliffs, NJ: Prentice Hall; 2006.

[17] Quarteroni A, Sacco R, Saleri F. Numerical mathematics, texts in applied mathematics. 2nd ed. Berlin, Heidelberg: Springer; 2007.

[18] Romero LA, Ghiglia DC, Ober CC, Morton SA. Phase encoding of shot records in prestack migration. Geophysics 2000;65:426–36.

[19] Stokoe II KH, Wright SG, Bay JA, Roësset JM. Characterization of geotechnical sites by SASW method. In: Woods RD, editor. Geophysical characterization of sites. New Delhi, India: Oxford & IBH Pub. Co.; 1994. p. 15–25.

[20] Tröltzsch F. Optimal control of partial differential equations: theory, methods, and applications, graduate studies in mathematics, vol. 112. American Mathematical Society; 2010.

[21] Vogel CR. Computational methods for inverse problems, frontiers in applied mathematics. Philadelphia, PA: Society for Industrial and Applied Mathematics (SIAM); 2002.